



# A dual defect co-modified S-scheme heterojunction for boosting photocatalytic CO<sub>2</sub> reduction coupled with tetracycline oxidation

Xuemei Jia<sup>a,b</sup>, Cheng Hu<sup>a,b</sup>, Haoyu Sun<sup>a,b</sup>, Jing Cao<sup>a,b</sup>, Haili Lin<sup>a,b,\*</sup>, Xinyue Li<sup>a,b</sup>, Shifu Chen<sup>a,b,\*</sup>

<sup>a</sup> College of Chemistry and Materials Science, Huaibei Normal University, Huaibei, Anhui 235000, PR China

<sup>b</sup> Key Laboratory of Green and Precise Synthetic Chemistry and Applications, Ministry of Education, Huaibei Normal University, Huaibei, Anhui 235000, PR China

## ARTICLE INFO

### Keywords:

Dual-defect  
S-scheme  
I doped BiOBr/N vacancy g-C<sub>3</sub>N<sub>4</sub>  
Photocatalytic  
Dual-purpose reaction system

## ABSTRACT

To synchronously relieve energy shortage and wastewater remediation, herein, a dual-defect S-scheme heterojunction of I doped BiOBr modified N vacancy g-C<sub>3</sub>N<sub>4</sub> (labeled as IB/CNx) was designed for simultaneously photocatalytic CO<sub>2</sub> reduction coupled with tetracycline oxidation. The 70IB/CNx presented higher photocatalytic property for CO<sub>2</sub> reduction coupled with TC removal than those of IB/CN, BiOBr/CNx, and BiOBr/CN. The improved photocatalytic activity was mainly attributed to the synergistic effect of doped I ions and N defects. Besides, such designed coupled reaction system presented much superior catalytic performance than those of two half-reactions, which achieved the full utilization of carriers. All in all, a dual-defect heterojunction enhanced a dual-function reaction system, in which the dual-defect active spots accelerated the transfer and separation of carriers, meanwhile, the dual-function reaction system realized the full utilization of the charges. This work highlighted the pivotal role of defect engineering to design efficient photocatalysts for environment and energy applications.

## 1. Introduction

Environmental and energy issues have become a significant challenge for scientific community and international societies today. Photocatalytic technology is a promising and attractive solution to solve the above two difficult problems. In especial, solar energy driven CO<sub>2</sub> reduction into usable fuels, as a potential way, mitigates the energy crisis and greenhouse effect [1–5]. Photocatalytic reduction of CO<sub>2</sub> integrated with oxygen (O<sub>2</sub>) production from the oxidation of pure water has been regarded as a perfect reaction system [1,6]. Nevertheless, the O<sub>2</sub> generation was difficult and almost no reports because of its sluggish reaction kinetics and hard desorption [7]. Besides, such photocatalytic systems frequently suffered from low separation efficiency electron-hole (e<sup>-</sup>-h<sup>+</sup>) pairs and poor activity. Sacrificial reagents, such as ascorbic acid, sodium sulfite, isopropyl alcohol and triethanolamine (TEOA), etc. were utilized to overcome the above problems, which not only produced unexpected by-products, but also wasted the oxidation power of h<sup>+</sup> [4].

Lately, the CO<sub>2</sub> reduction coupling organics oxidation synthesis have been considered as a resultful method to overcome the above-mentioned troubles, which not only implemented the complete utilization of

carriers, but also generated high-valued chemicals [8–14]. Nevertheless, the by-products and residual organic solvents brought serious environmental pollution, which is a huge challenge for coupled reaction systems. Thus, it is quite requisite to probe an ideal coupled reaction system, which could not only available purify the environment, but also alleviate the energy crisis. According to the principle of the coupled reaction system, “doing the opposite”, that is, starting from the reverse oxidation semi-reaction of the above coupling reaction system. In other words, the “organic pollution mineralization” replaced with “traditional fine chemical synthesis”, which combined with CO<sub>2</sub> reduction to construct new coupling reaction system. The construction of the coupled reaction system for CO<sub>2</sub> reduction coupled organic pollution mineralization could be considered as an ideal coupling reaction system, which not only realized the full utilization of carriers, but also achieved the purpose of win-win results between energy and environment.

To realize the above coupling reaction system, it is quite indispensable to legitimately design a high-efficiency photocatalysts with sufficient active sites, strong oxidation reduction potential and speedy separation rate of carriers for such synergetic coupling of CO<sub>2</sub> reduction and organic pollution removal in one reaction. Newly, BiOBr, as typical

\* Corresponding authors at: College of Chemistry and Materials Science, Huaibei Normal University, Huaibei, Anhui 235000, PR China.

E-mail addresses: [linhaili@mail.ipc.ac.cn](mailto:linhaili@mail.ipc.ac.cn) (H. Lin), [chshifu@chnu.edu.cn](mailto:chshifu@chnu.edu.cn) (S. Chen).

<https://doi.org/10.1016/j.apcatb.2022.122232>

Received 20 September 2022; Received in revised form 13 November 2022; Accepted 26 November 2022

Available online 28 November 2022

0926-3373/© 2022 Elsevier B.V. All rights reserved.

semiconductor, has gained widespread concerns due to unique layered structure, suitable band gap energy, favorable structural, good photochemical stability and especially strong oxidizing ability [15–17]. Nevertheless, the weak light absorption limited its visible light photocatalytic activity. Recently, iodine ion doping, such as  $\text{BiOI}_{1-x}\text{Br}_x$  [18–20],  $\text{Bi}_5\text{O}_7\text{Br}_{0.5}\text{I}_{0.5}$  [21],  $\text{BiOCl}_{1-x}\text{I}_x$  [22] and  $\text{BiO}(\text{ClBr})_{(1-x)/2}\text{I}_x$  [23], has been reported as an effective strategy to overcome the above-mentioned inherent shortcomings, which not only can effectively expand the visible light absorption, but also can narrow band gap, thereby improving the photocatalytic activity. Although I doped BiOBr (labeled as IB) can effectively ameliorate the photocatalytic performance, it is fairly difficult for single-component IB photocatalysts to realize the above coupled reaction system owing to the swift recombination rate of carriers and weak reduction potential ( $\approx 0.29$  eV), which is determined by its inherent band alignment [19]. Recently, a typical S-scheme heterojunction has been considered as one of the most promising approaches to solve the above problems, which was proposed by Yu et al. [24]. The S-scheme heterojunction is primarily consisted of oxidation photocatalyst (PC I) and reduction photocatalyst (PC II). In S-scheme system, the unserviceable electrons on the conduction band (CB) of PC I and the futile holes on the valence band (VB) of PC II could be recombined at the interface. On the contrary, the electrons with strong reduction power and holes with high oxidation ability could be retained on the CB of PC II and VB of PC I, respectively [25–27]. Thus, the construction of IB-based S-scheme heterojunctions could serve as a desired system for photocatalytic  $\text{CO}_2$  reduction coupled with organic pollution oxidation, which not only expedited the separation of electrons and holes, but also preserved the strong redox ability of photoinduced carriers. Since IB with a relatively positive valence band potential ( $E_{\text{VB}}$ ) was considered as an oxidation-type photocatalyst [19], which could constitute S-scheme heterojunction with a reduction-type photocatalyst.

Up to now, graphitic carbon nitride ( $\text{g-C}_3\text{N}_4$ ), as a metal-free polymer, has been extensively researched in the field of photocatalysis due to its facile preparation, chemical stability and especially strong reduction potential ( $E_{\text{CB}} \approx -1.0$  eV), which has been extensively studied for photocatalytic  $\text{CO}_2$  reduction [28–32]. Although  $\text{g-C}_3\text{N}_4$  had the strong enough reduction ability for  $\text{CO}_2$  reduction, it is hard for  $\text{g-C}_3\text{N}_4$  to achieve the high-efficient photocatalytic performance of  $\text{CO}_2$  reduction due to the limited active sites [30]. Lately, some literatures implied that the introduction of N defects in  $\text{g-C}_3\text{N}_4$  (denoted as  $\text{CN}_x$ ) could obviously heighten its photocatalytic performance by providing more active sites, expanding the visible light response and capturing electrons [33–36]. For instance, Yu et al. confirmed that the N-deficient  $\text{g-C}_3\text{N}_x$  not only extended obviously spectral adsorption, but also increased more reactive sites [33]. Majima's group reported that the nitrogen vacancies as electron trap states in  $\text{g-C}_3\text{N}_4$  presented outstanding photocatalytic  $\text{H}_2$  evolution [34]. Most importantly,  $\text{CN}_x$  as a reduction type semiconductor with more negative  $E_{\text{VB}}$  could combine with the IB to form a dual defective S-scheme heterojunction, which was expected to present synergistic effect on optimizing the photocatalytic performance for  $\text{CO}_2$  reduction coupled with TC degradation.

Hence, a dual-defect I doped BiOBr modified N vacancy  $\text{g-C}_3\text{N}_4$  (donated as IB/ $\text{CN}_x$ ) S-scheme heterojunction was constructed, in which activated N-defect sites of  $\text{g-C}_3\text{N}_4$  acted as abundant active sites for reduction half-reaction, meanwhile, I doped BiOBr with strong oxidizing capacity participated in the oxidation half-reaction, thereby, maximizing the separation efficiency of carriers for efficient photocatalytic  $\text{CO}_2$  reduction coupled with TC degradation. Besides, the dual defective system obviously advanced the photocatalytic activity and stability of dual-function reaction system, in which the dual-defect active spots accelerated the transfer and separation of carriers, meanwhile, the dual-function reaction system realized the full utilization of charges. The mechanism of cooperative effect was discussed deeply according to theoretical calculation and experiments. This work provided a novel insight into the research of dual defect heterojunction photocatalysts for

dual-functional coupled reaction system, and further verified the latent application of photocatalytic  $\text{CO}_2$  reduction coupled with contaminants removal.

## 2. Experimental

### 2.1. Synthesis of catalysts

Firstly, the N vacancy  $\text{g-C}_3\text{N}_4$  (labeled as  $\text{CN}_x$ ) nanosheets were successfully synthesized via calcining dicyandiamide at  $550^\circ\text{C}$  for 4 h with the heating rate of  $1^\circ\text{C}/\text{min}$  under  $\text{N}_2$  atmosphere. Subsequently, the as-obtained sample was cooled to room temperature and then ground into powder. As a contrast, the bulk  $\text{g-C}_3\text{N}_4$  (denoted as CN) was fabricated in the absence of  $\text{N}_2$  atmosphere under the same conditions.

Afterwards, a series of dual-defect I doped BiOBr/N vacancy  $\text{g-C}_3\text{N}_4$  heterojunctions (named as IB/ $\text{CN}_x$ ) were synthesized by simple deposition-precipitation method. In brief, 0.485 g of  $\text{Bi}(\text{NO}_3)_3 \cdot 5\text{H}_2\text{O}$  (1 mmol) was dissolved into 20 mL of glacial acetic acid solution ( $\text{pH} = 1.96$ ). Subsequently, 0.44 g of  $\text{CN}_x$  was uniformly dispersed in the clarified solution as described above. Then, a quantity of aqueous solution containing 0.0978 g of NaBr (0.95 mmol) and 0.0083 g of KI (0.05 mmol) was slowly dropped and stirred for 3 h at room temperature. Finally, the precipitate was collected, washed several times with deionized water and ethanol and then dried at  $80^\circ\text{C}$  for 12 h in air. The as-obtained photocatalyst was named as 70 wt% IB/ $\text{CN}_x$  (labeled as 70IB/ $\text{CN}_x$ ).

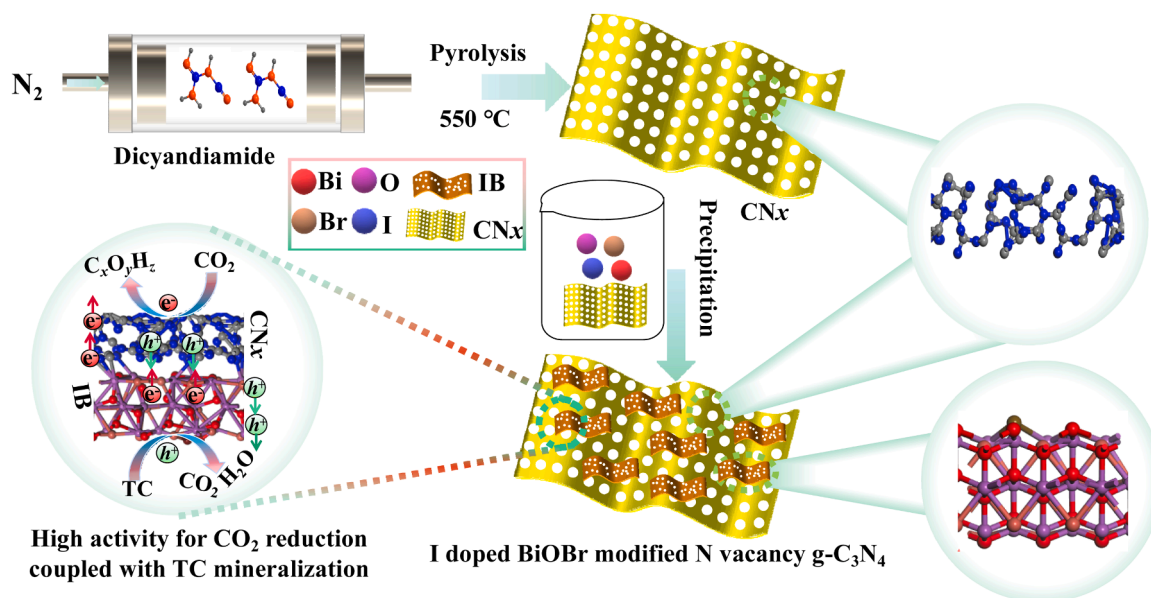
Likewise, a range of  $n\text{IB}/\text{CN}_x$  composites with different weight ratios were obtained by changing the amount of  $\text{CN}_x$ , and the weight ratios ( $n$ ) of I doped BiOBr/ $\text{CN}_x$  were set as  $n = 30, 50, 90$  and 110 wt%, which were marked as 30IB/ $\text{CN}_x$ , 50IB/ $\text{CN}_x$ , 90IB/ $\text{CN}_x$  and 110IB/ $\text{CN}_x$ , respectively. The preparation process of dual-defect I doped BiOBr/N vacancy  $\text{g-C}_3\text{N}_4$  heterojunction photocatalyst was presented in Scheme 1.

As a reference, the I doped BiOBr sample (labeled as IB) was prepared by utilizing the similar synthesis process to the IB/ $\text{CN}_x$  heterojunctions without the addition of  $\text{CN}_x$ . For comparison, BiOBr catalyst was similarly prepared as the preparation of IB sample in the absence of KI.

As a contrast, the details preparation of 70 wt% BiOBr/CN, 70 wt% IB/CN and 70 wt% BiOBr/ $\text{CN}_x$  were provided in the Electronic Supporting Information (ESI), which were named as 70B/CN, 70IB/CN and 70B/ $\text{CN}_x$ , respectively.

### 2.2. Characterizations

A Bruker D8 Advance X-ray diffractometer (XRD) was applied to detect the crystal structures of catalysts. The ZEISS Sigma 300 scanning electron microscopy (SEM) and the JEOL F200 transmission electron microscopy (TEM) was used to observe the micro-morphologies of samples. A Shimadzu UV-3600 iplus UV–vis spectrophotometer (DRS) was carried out to record the light absorption properties of photocatalysts. The Bruker EMX plus paramagnetic resonance spectrometer (EPR) was operated to measure the reactive radicals and vacancies. Quantitative EPR results were measured by using 10 mg of catalysts. The concentration of defect was detected through referring to the spin concentration of the lone electrons of  $\text{Cr}^{3+}$  using  $\text{MgO}$  calibration. Subsequently, the calibration of unit mass was used as a standardized sample to acquire the conversion coefficient between the molar quantities of spin electrons and EPR peak areas. Ultimately, the defect concentration trapping one electron in the as-obtained samples was calculated by utilizing the conversion coefficient according to the EPR peak areas. A PHI5000 Versa Probe III X-ray photoelectron spectrometer (XPS) was implemented to analyze the in situ irradiated XPS spectra. The Micro-meritics ASAP2460 surface area analyzer was used to record the specific surface area and  $\text{CO}_2$  adsorption of samples. The Bruker INVENIO RFT-IR spectrometer was utilized to conduct the Fourier transform infrared (FT-IR) and in situ FT-IR spectra. The Edinburgh Instruments FLS1000



Scheme 1. Scheme of the preparation procedure of I doped BiOBr/CNx.

fluorescence spectrometer was carried out to test the time-resolved fluorescence (TRPL) decay curves and steady state photoluminescence (PL) spectra. The intermediates of TC degradation were determined using a Thermo Scientific Ultimate 3000 UHPLC-Q Enactive liquid chromatograph-mass (LC-MS) spectrometry. The isotope-labelled  $^{13}\text{CO}_2$  test was evaluated using an Agilent 7890A-Agilent 5975 C gas chromatograph-mass (GC-MS) spectrometry.

### 2.3. Photocatalytic measurements

Photocatalytic  $\text{CO}_2$  reduction coupled with TC oxidation was detected in a MC-SPB10-AG  $\text{CO}_2$  reaction system (Beijing MerryChange Technology Co., Ltd) utilizing a MC-PF300C 300 W Xe lamp as illuminant. Briefly, 50 mg of sample was dispersed in 50 mL of 20 mg  $\text{L}^{-1}$  TC aqueous solution by 5 min of ultrasonication. Afterwards, the reaction system was hinged to the reactor and vacuumized. Subsequently, 50 mL of  $\text{CO}_2$  as a reaction gas was poured into the system. The temperature of reaction was consistently maintained at 5 °C. A gas chromatograph (FuLi, GC9790II) was carried out to test the gas product. At length, 5 mL of suspension was sampled and then centrifuged to take supernatant. Ultimately, the supernatant was performed on a UV-vis spectrophotometer (DRS, Shimadzu, UV-3600 iplus).

The action spectra for CO and  $\text{CH}_4$  production were investigated on the as-obtained samples under the same condition of photo-redox reaction using a 300 W xenon lamp equipped with monochromatic light at 400, 420, 450, 500, 550, 600, 650, 700 and 750 nm. The apparent quantum efficiency (AQE) of monochromatic wavelength as a function was calculated according to the ratio of the number of electrons consumption (rate of CO and  $\text{CH}_4$  evolution) to the flux of incident photons in the system. The corresponding calculation formula of AQE was presented as follows [37,38]:

$$\text{AQE}(\%) = \frac{N(\text{solar fuels}) \times N_0}{N(\text{Photon})} \times 100\%$$

$$= \frac{[2 \times n(\text{CO}) + 8 \times n(\text{CH}_4)] \times N_0}{\frac{PST\lambda}{hc}} \times 100\%$$

Where  $N(\text{solar fuels})$ ,  $N(\text{photon})$  and  $N_0$  expressed as the mole number of evolved solar fuels, number of incident photons and Avogadro constant, respectively. The  $n(\text{CO})$  and  $n(\text{CH}_4)$  represented the mole number of evolved CO and  $\text{CH}_4$ , respectively. In addition,  $S$ ,  $P$  and  $t$  indicated as the light radiation area, power of light and illumination time, respectively.

### 2.4. Photoelectrochemical tests

Electrochemical impedance spectrum (EIS), photocurrent responses, and Mott-Schottky (M-S) curves were measured on a CHI 660E electrochemical workstation using 0.5 M  $\text{Na}_2\text{SO}_4$  solution as electrolyte solution. The counter and reference electrodes were platinum plate and Ag/AgCl, respectively. The working electrode was manufactured on the basis of the following steps: Firstly, 3 mg of sample was dispersed into 2 mL of mixture containing ethanol/distilled water/Nafion and sonicated for 30 min to form uniform suspension. Next, 0.2 mL of suspension liquid was sprayed on  $1 \times 1$  cm conductive glass and dried naturally.

### 2.5. Density functional theory (DFT) calculations

All the density functional theory calculations were performed by using the Vienna ab initio Simulation Program (VASP) [39,40]. The generalized gradient approximation (GGA) in the Perdew-Burke-Ernzerhof (PBE) form and a cutoff energy of 500 eV for planewave basis set were adopted [41]. A  $3 \times 3 \times 1$  Monkhorst-Pack grid was used for sampling the Brillouin zones at structure optimization [42]. The ion-electron interactions were described by the projector augmented wave (PAW) method. The convergence criteria of structure optimization were chosen as the maximum force on each atom less than 0.01 eV/Å with an energy change below  $1 \times 10^{-5}$  eV. The DFT-D3 semiempirical correction was described via Grimme's scheme method.

The  $\text{CO}_2$  adsorption energies ( $E_{\text{ads}}$ ) on the surface of pure IB, CNx and two sides of IB/CNx heterojunction were defined according to  $E_{\text{ads}} = E_{\text{tot}} - E_{\text{slab}} - E_{\text{CO2(g)}}$ , where  $E_{\text{CO2(g)}}$ ,  $E_{\text{slab}}$ ,  $E_{\text{tot}}$  were the energies of independent  $\text{CO}_2$  molecules, clean surface, and  $\text{CO}_2$  adsorbed on the surface, respectively.

The Gibbs free energy change ( $\Delta G$ ) for each elemental step was defined by  $\Delta G = \Delta E + \Delta \text{ZPE} - T\Delta S + \Delta G_U + \Delta G_{\text{pH}}$ , where  $\Delta E$  and  $\Delta \text{ZPE}$  were the adsorption energy based on density functional theory calculations and the zero-point energy correction, respectively.  $T$ ,  $\Delta S$ ,  $U$ , and  $\Delta G_{\text{pH}}$  represented the temperature, the entropy change, the applied electrode potential, and the free energy correction of the pH, respectively.

### 3. Results and discussion

#### 3.1. Characterization results of samples

The crystallographic structure of materials was examined preliminarily by XRD. Fig. 1a displayed that pristine BiOBr was well-defined by the characteristic diffraction peaks of tetragonal BiOBr (JCPDS 09–0393). After introducing of  $I^-$ , the (102) and (110) diffraction peaks of IB shifted slightly to lower angle, indicating that the  $I^-$  was successfully implanted into BiOBr lattice by replacing  $Br^-$  with smaller ionic radius [43]. An opposite phenomenon appeared on the CNx, the (002) peak of CNx shifted towards higher angle than that of CN because the N species disappeared from CN framework [44]. When IB was coupled with CNx (Fig. 1b), a mixed diffraction peaks of IB and CNx appeared in IB/CNx composites. Moreover, as the amount of IB increased, the peak intensities of IB increasingly strengthened while those of CNx gradually reduced, which further affirmed the coexistence of IB and CNx. In addition, the XRD peaks of 70B/CN (Fig. S1a), 70IB/CN (Fig. S1b) and 70B/CNx (Fig. S1c) heterojunctions were further confirmed the formation of heterojunction. Subsequently, the major functional groups present in the as-obtained materials were detected by FT-IR. As shown in Fig. S2, the peak of bare BiOBr was located at  $517\text{ cm}^{-1}$ , assigning to the stretching vibrations of Bi-O bonds [45,46]. After introducing  $I^-$ , the characteristic peaks of the IB revealed no obvious difference with that of BiOBr. A similar phenomenon appeared on the CNx, the absorption bands located at  $809\text{ cm}^{-1}$  and  $1210\text{--}1634\text{ cm}^{-1}$  were deemed to the triazine units and C-N heterocycles in the CNx, respectively [46,47], which were basically agreement with the characteristic peaks of CN. Once IB coupled with CNx, the stretching modes of Bi-O bonds and C-N heterocycles coexist in the IB/CNx hybrids, illustrating that the IB/CNx heterojunctions have been successfully constructed.

To confirm the existence of defect in samples, the EPR spectra of BiOBr, IB, CN and CNx were carried out. As illustrated in Fig. 1c, the strong EPR signals were found in IB at around  $g = 2.004$ , instead, there

is almost no EPR signal in BiOBr. A similar phenomenon occurred in the CNx, the EPR signal was much higher than that of CN. These outcomes indicated that the vacancies were formed in IB and CNx. Besides, the defect quantification of samples was analyzed and presented in Fig. 1d. The defect concentration of BiOBr, IB, CN and CNx were  $1.2e^{11}$ ,  $3.88e^{12}$ ,  $3.2e^{11}$  and  $9.99e^{12}$ , deducing that the introduction of defects provided more unsaturated sites on the surface of photocatalysts.

The microstructures of catalysts were examined via SEM. Pristine BiOBr (Fig. 2a) and IB (Fig. 2b) exhibited the similar hierarchical micro flower structures, which were composed of massive nanosheets. The morphology of CNx (Fig. 2d) evidently changed to nanosheets from the bulk structure of CN (Fig. 2c). After introducing BiOBr into bulk CN (Fig. 2e), it could be observed that many BiOBr nanosheets randomly spread on the surface of CN. A similar morphology emerged in the 70IB/CNx composite (Fig. 2f). In addition, the morphology of IB, CNx and 70IB/CNx were also tested by TEM (Fig. 2g-i). It could be seen from Fig. 2i that numerous IB nanosheets firmly connected with CNx nanosheets in 70IB/CNx, which were in accord with SEM observation. To confirm the interface formation between IB and CNx, the corresponding HRTEM images of IB, CNx and 70IB/CNx were given in Fig. 2j-l. It could be observed from Fig. 2j that IB had a well-defined lattice spacing of  $0.284\text{ nm}$ , corresponding to (102) plane of IB. On the contrary, no lattice spacings were found in CNx (Fig. 2k) due to its amorphous structure, which was consistent with reported in the literature [48]. As for 70IB/CNx heterojunction (Fig. 2l), a well-defined interplanar spacings with  $0.284\text{ nm}$  was discovered, which could be assigned to the (102) plane of IB. Besides, the dim and disordered layer could be obviously observed at the sample edges due to the existence of CNx. The above results confirmed that the heterojunction interface was indeed formed. Besides, STEM elemental mapping images of 70IB/CNx were presented in Fig. 2m, it can be found that Br, I, Bi, O, C and N elements evenly distributed onto 70IB/CNx photocatalyst.

The optical absorption properties of photocatalysts were recorded by UV-vis DRS spectra, which was delineated in Fig. 3a. Compared to pure

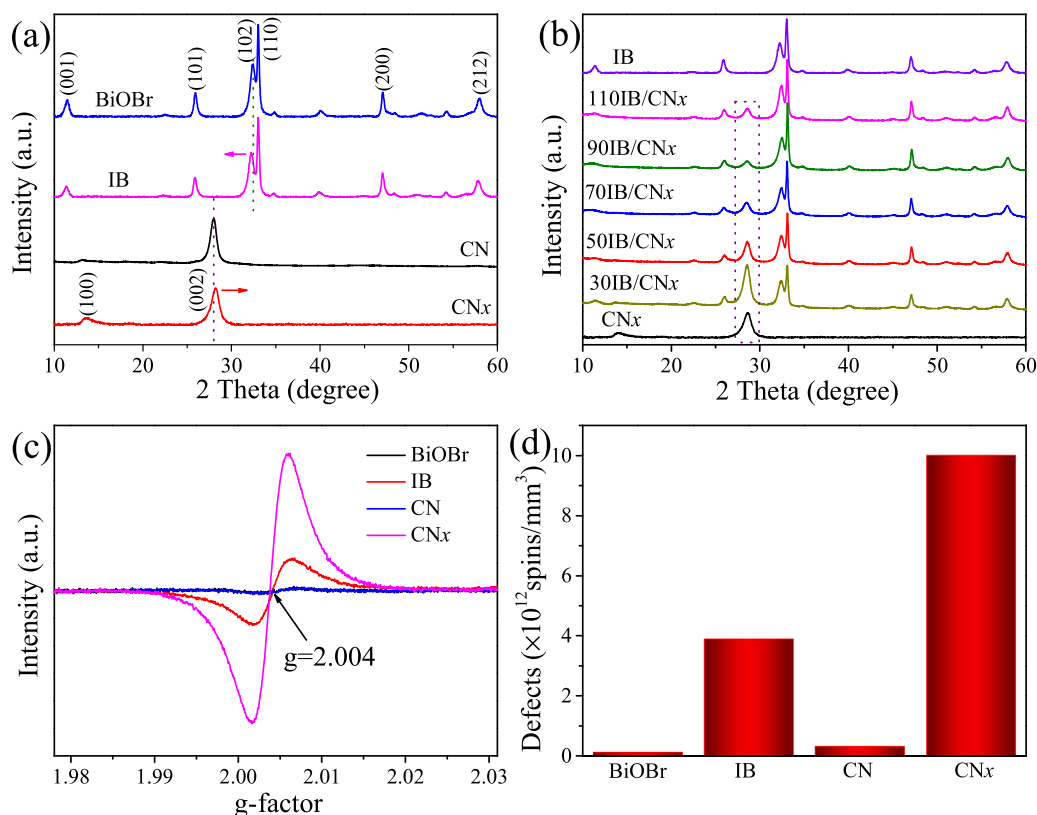


Fig. 1. (a, b) XRD patterns, (c) EPR spectra and (d) defects concentration of the as-obtained samples.



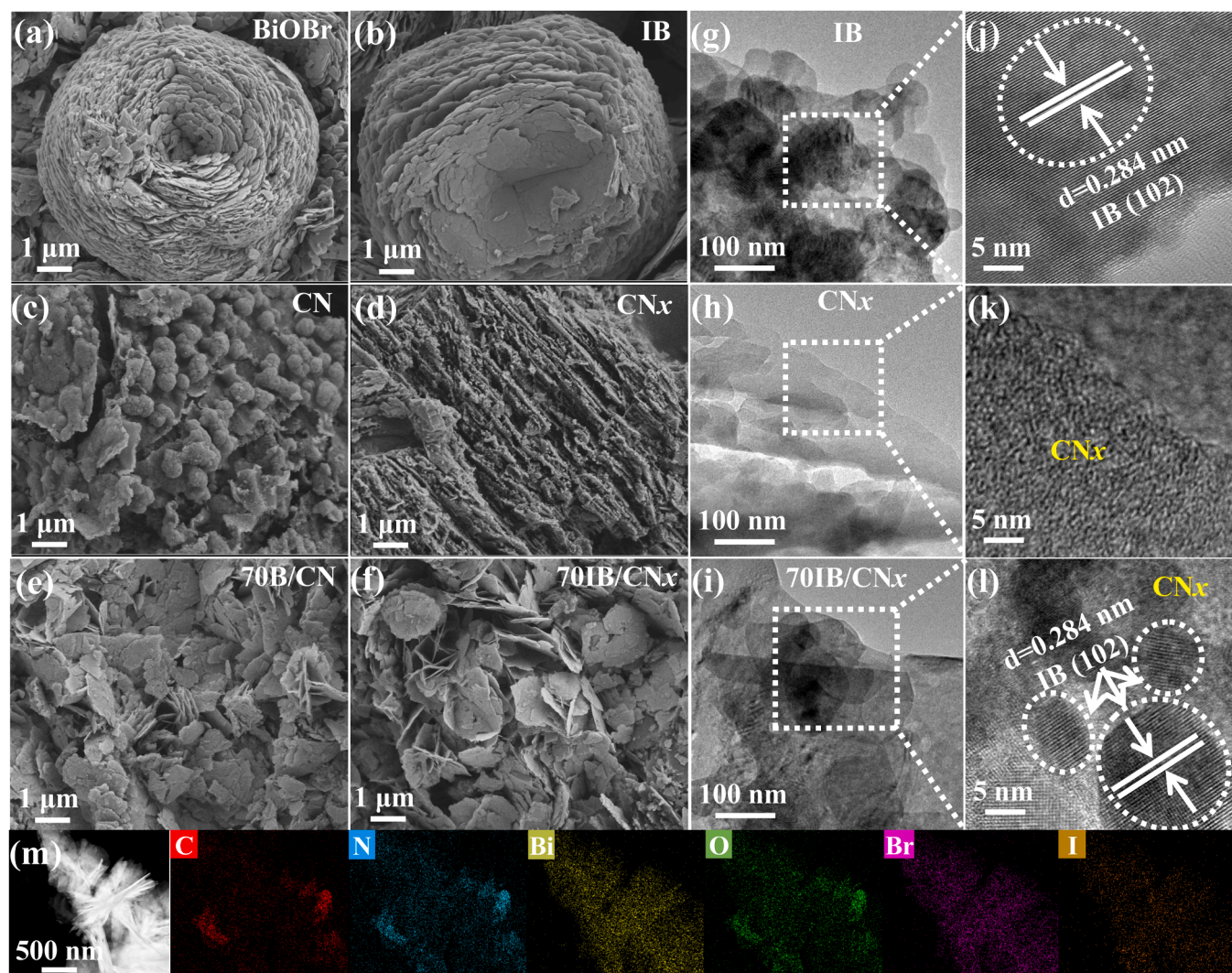


Fig. 2. SEM images of (a) BiOBr, (b) IB, (c) CN, (d) CNx, (e) 70B/CN and (f) 70IB/CNx; TEM images of (g) IB, (h) CNx and (i) 70IB/CNx; HRTEM images of (j) IB, (k) CNx and (l) 70IB/CNx; (m) STEM elemental mapping of 70IB/CNx composite.

BiOBr, the absorption edge of IB was obviously broadened to 511 from 433 nm. Similarly, the introduction of N defects also expanded light response range of CNx. After the coupling of IB and CNx, the optical absorption of 70IB/CNx heterojunction did not apparently enhance, however, a small increase situated between 480 and 511 nm. Moreover, as the loading amount of IB increased, the optical absorption edges of IB/CNx slightly red-shifted, which were presented in Fig. S3a. In addition, 70IB/CNx displayed broader light absorption tail than that of 70B/CN, 70IB/CN, and 70IB/CN (Fig. S3b), which was mainly attributed to the synergistic effect of the  $\Gamma^-$  doping and N defects.

Subsequently, the band gap energies ( $E_g$ ) of BiOBr, IB, CN and CNx were calculated on the basis of Tauc's formula  $ah\nu = A(h\nu - E_g)^{n/2}$  [19]. The  $n$  values of BiOBr, IB, CN and CNx were taken as 4 owing to their indirect semiconductor characters [43,48]. Consequently, the  $E_g$  values of BiOBr, IB, CN and CNx were 2.72, 2.22, 2.61 and 2.33 eV, respectively (Fig. 3b). Besides, the M-S curves (Fig. 3c) were conducted to infer the flat-band potentials ( $E_{fb}$ ) of BiOBr, IB, CN and CNx. The positive slopes of the M-S plots indicated that they were  $n$  type semiconductors. The  $E_{fb}$  values of BiOBr, IB, CN and CNx were  $-0.48$ ,  $-0.30$ ,  $-0.95$  and  $-0.88$  V vs Ag/AgCl ( $-0.28$ ,  $-0.10$ ,  $-0.75$  and  $-0.68$  V vs NHE), respectively [49]. Accordingly, the  $E_{CB}$  of BiOBr, IB, CN and CNx were  $-0.38$ ,  $-0.20$ ,  $-0.85$  and  $-0.78$  eV, respectively, because the  $E_{CB}$  of  $n$ -type semiconductor was 0.10 V more negative than that of  $E_{fb}$ . The VB potentials ( $E_{VB}$ ) were calculated to be 2.34, 2.02, 1.76 and 1.55 eV

according to the function  $E_{VB} = E_{CB} + E_g$  [49]. Furthermore, the  $E_{VB}$  of BiOBr, IB, CN and CNx were further confirmed by valence-band XPS (VB-XPS) spectra (Fig. 3d). The  $E_{VB}$  of BiOBr, IB, CN and CNx from the VB-XPS spectra were 2.51, 2.05, 1.85 and 1.55 eV, respectively, which were close to those from the M-S curves. In order to observe the energy band structure of IB/CNx more clearly, a schematic diagram of the corresponding energy band structures of BiOBr, IB, CN and CNx was presented in Fig. S4. For pure BiOBr, the  $E_g$  values were 2.72 eV. After introducing  $\Gamma^-$  into BiOBr, the  $E_g$  values of BiOBr significantly decreased by 0.5 eV. A similar phenomenon occurred on CNx, the band gap energy of CNx was significantly lower than that of CN owing to the presence of N defects. It was deduced that the defect engineering could act as an effective strategy to regulate the energy band structure of BiOBr and CN. More importantly, both of IB and CNx could be more easily excited by the visible light in virtue of their narrow band gap energies. Apparently, IB/CNx presented a staggered energy band structure, which was conducive to the separation and migration of photoinduced carriers.

The band structure and the corresponding density of states (DOS) of BiOBr, IB and CNx was manifested by DFT calculation. As shown in Fig. 4a, the band gap of BiOBr was around 1.13 eV. Moreover, the corresponding DOS illustrated that the CB was mainly derived from the Bi 6p state, and the VB was primarily contributed by Br 5p orbital. After  $\Gamma^-$  doping, the CB of IB was dominated by Bi 6p, which hybridized with trace amounts of O 2p and Br 5p, and the VB was mainly O 2p hybridized

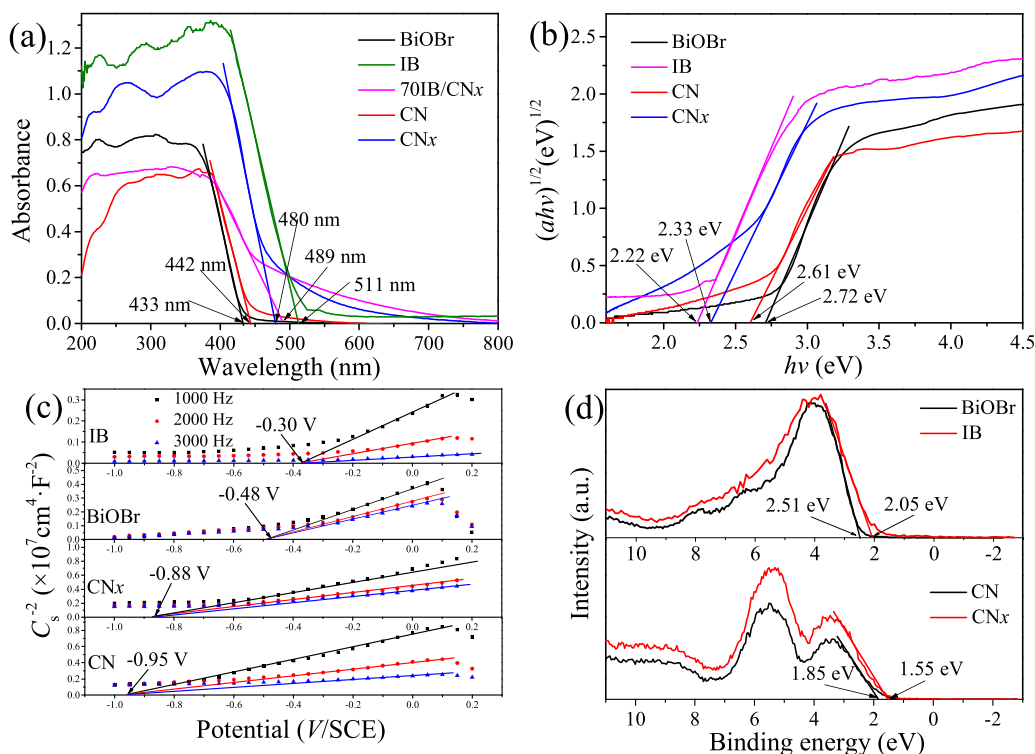


**Fig. 3.** (a) UV-vis DRS of the as-obtained samples; (b) Band gap energies, (c) Mott-Schottky (M-S) plots, and (d) valence-band XPS (VB-XPS) spectra of BiOBr, IB, CN and CNx.

with a tiny amount of Bi 6p and Br 5p (Fig. 4b). Except for the hybridizations of Bi 6p, O 2p and Br 5p to VB, a small amount of I 5p participated in the hybridization of VB in IB, resulting in the tiny narrowing of bandgap compared to BiOBr. For CNx (Fig. 4c), the CB was chiefly dominated by C 2p orbital, which hybridized with C 2s, N 2s and N 2p, while the VB basically consisted of N 2p and N 2s state, which hybridized with a spot of C 2s and C 2p. The above calculations indicated that the introduction of doping  $\text{I}^-$  ions and N defect into IB/CNx sample not only expanded the visible light absorption and promoted the separation of carriers, but also increased more surface-active sites, thereby, improving effectively the photocatalytic activity.

### 3.2. Photoredox reaction and mechanism of $\text{CO}_2$ reduction with TC removal

To simulate the green photocatalytic reaction system, the  $\text{CO}_2$  photoreduction coupled with TC degradation in a cooperative catalytic system was performed under visible light irradiation ( $\lambda > 420 \text{ nm}$ ). The pristine BiOBr displayed low photocatalytic activity towards  $\text{CO}_2$  reduction due to the swift recombination of carriers and weak reduction capacity. After the introduction of  $\text{I}^-$ , the CO and  $\text{CH}_4$  productions over IB both increased linearly as extending of the light exposure time (Fig. 5a and b). An analogous phenomenon occurred in the CNx, the CNx exhibited an enhanced photocatalytic activity compared with bulk CN. This demonstrated that the introduction of defects could effectively ameliorate the photocatalytic performance. More importantly, the coupling of IB and CNx presented excellent activity for  $\text{CO}_2$  conversion and TC removal (Fig. 5c). Particularly, the 70IB/CNx heterojunction showed superior photocatalytic activity than that of IB and CNx, illustrating that the construction of heterojunctions effectively accelerated the separation and migration of carriers.

Except for heterojunction structures, the introduction of surface defects also played a pivotal role in improving the photocatalytic activity. As disclosed in Fig. 5d and Figs. S5a and b, in contrast with 70B/CN, 70IB/CN, and 70B/CNx photocatalysts, the 70IB/CNx sample

displayed an outstanding improvement for  $\text{CO}_2$  photoreduction coupled with TC degradation, implying that the synergistic effect of the double defects was also a vital factor to provide more active sites and accelerate separation of charges, thereby heightening the photocatalytic activity. As exhibited in Fig. S3b, although the light absorptions of 70B/CN, 70B/CNx and 70IB/CN were similar to those of 70IB/CNx, they presented a lower or higher photocatalytic properties under visible light ( $\lambda > 420 \text{ nm}$ ). To investigate the accurate visible range in which the modified samples were excited and reduced  $\text{CO}_2$ , the action spectra (AQE as a function of wavelength) over 70B/CN, 70B/CNx, 70IB/CN and 70IB/CNx were recorded in the range 400–750 nm, and were exhibited in Fig. S6a–d. It can be seen from Fig. S6a that the 70B/CN without defect presented low AQE. After the introduction of  $\text{I}^-$ , the AQE of 70IB/CN catalyst was evidently higher than that of 70B/CN sample (Fig. S6b). An analogous phenomenon appeared on the 70B/CNx (Fig. S6c), the AQE was significantly improved with the introduction of the N defects. Once the dual-defects were simultaneously introduced into the 70B/CN, the 70IB/CNx presented largest AQE (Fig. S6d), indicating that the synergistic effect of doped I ions and N defects could availably enhance the photocatalytic activity. Subsequently, the 70IB/CNx heterojunction was used as a model catalyst in the following experiments for further discussions.

Considering that the coupled reaction system may realize the complete utilization of carriers and thus affect the photocatalytic redox reactions. Thus, the effect of different reaction systems on 70IB/CNx was carried out. As expected, compared to two half-reactions of individual  $\text{CO}_2$  photoreduction and independent TC oxidation under Ar atmosphere, such designed coupled reaction system presented much superior catalytic performance than those of two half-reactions (Fig. 5e). The corresponding time courses of photocatalytic CO and  $\text{CH}_4$  generation were displayed in Figs. S7a and b. As discussed above, the construction of the coupled reaction system was another pivotal role in the enhanced catalytic activity. Moreover, the TOC value of the degradation product was further detected, and the mineralization rate was about 90.3%, implying that most of the TC had been completely mineralized to  $\text{CO}_2$



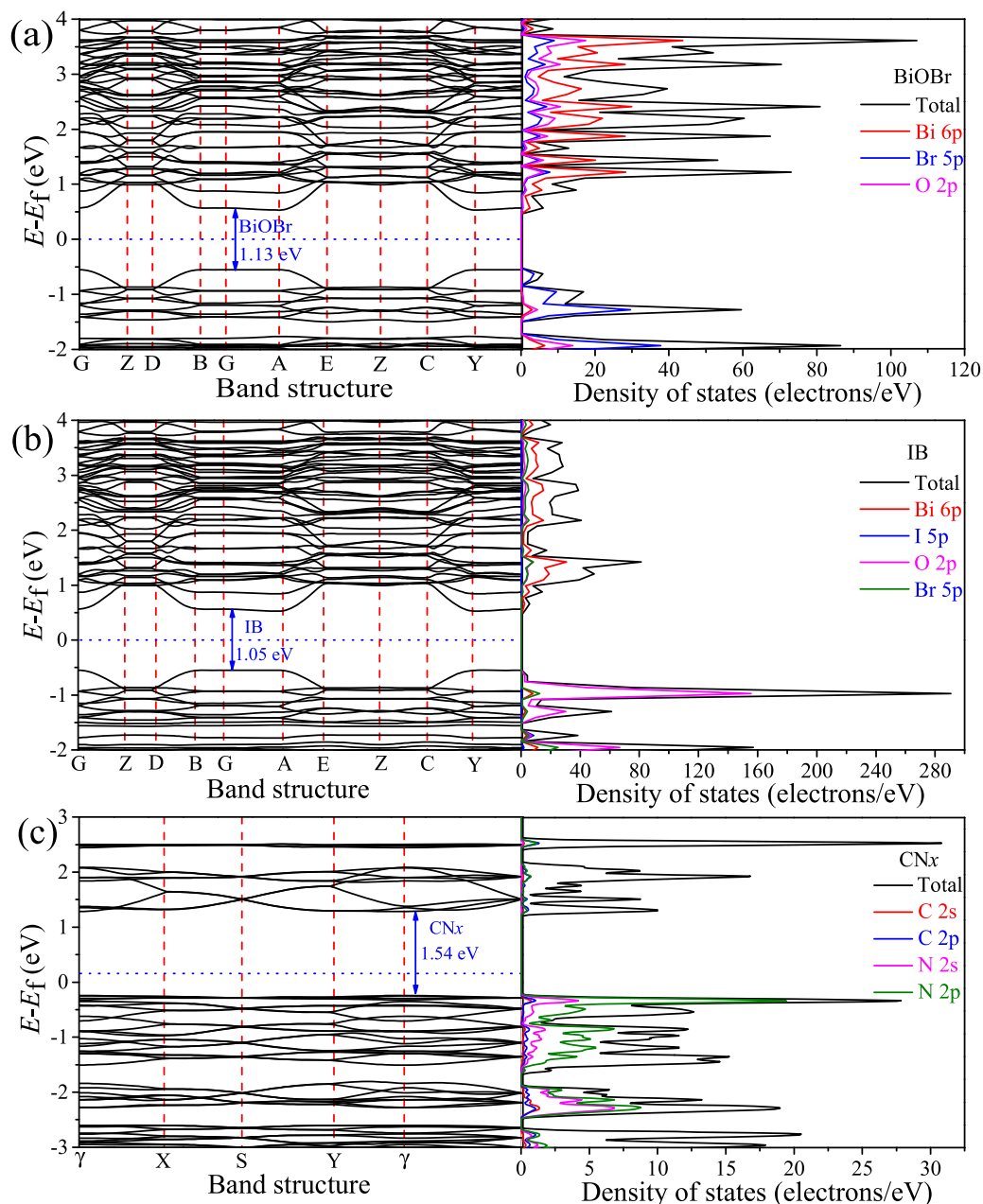
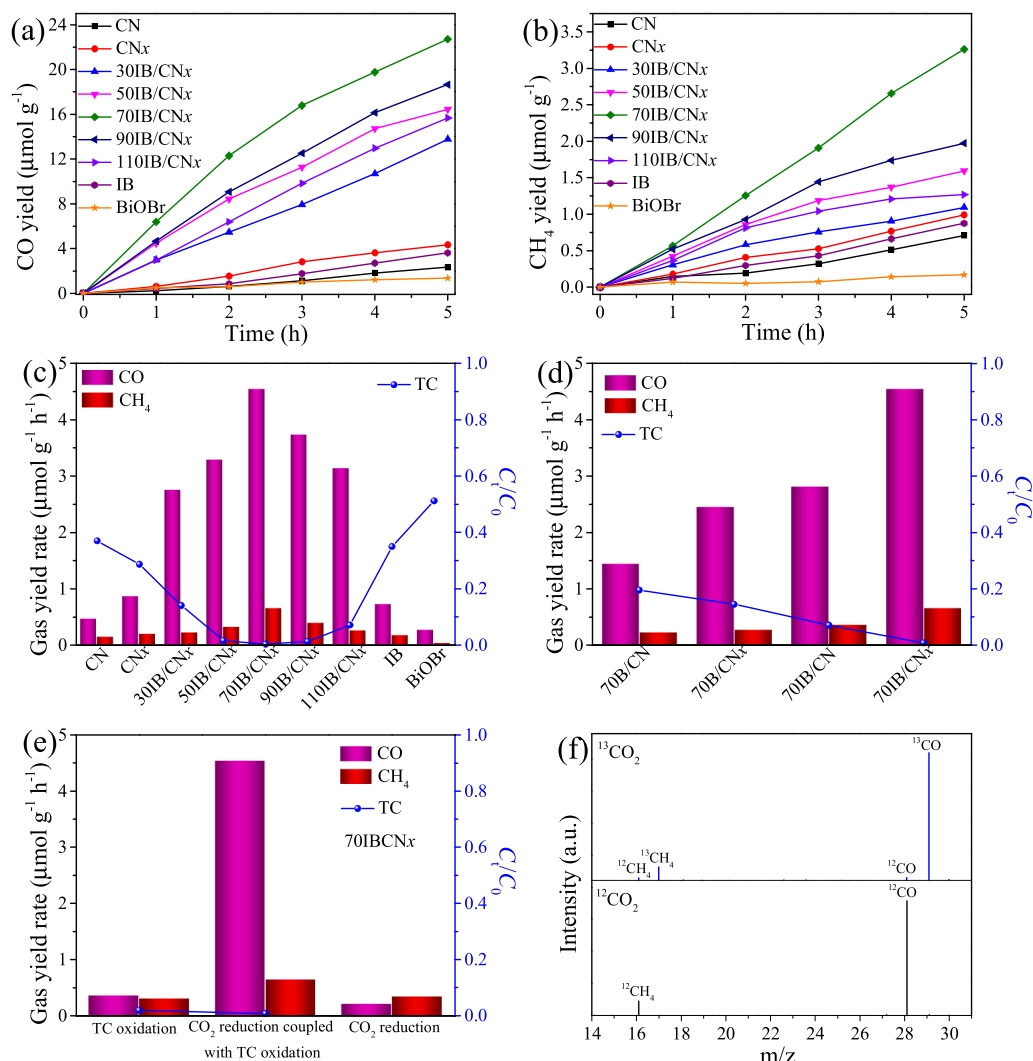


Fig. 4. Calculated band structures and DOS of (a) BiOBr, (b) IB and (c) CNx.

and  $H_2O$ , while trace amounts of TC was decomposed into small molecules. To further evaluate and discuss reaction mechanism, the mass balance between the products as a result of  $CO_2$  reduction and  $CO_2$  or intermediate generated degradation of TC was explored. Firstly, based on the TC mineralization rate combined with the amount of generated CO and  $CH_4$  from the half-reactions of independent TC oxidation under Ar atmosphere (Fig. 5e), the mass balance between the gas phase products and the  $CO_2$  of TC mineralization was discussed. As the above mentioned that the mineralization rate of  $20\text{ mg L}^{-1}$  TC ( $0.225\text{ }\mu\text{mol}$  of  $C_{22}H_{24}N_2O_8$ ) reached 90.3% after 5 h illumination, that is, the theoretically quantity of generated  $CO_2$  from TC decomposition was about  $4.45\text{ }\mu\text{mol}$ . Nevertheless, the amount of generated CO and  $CH_4$  from the half-reactions of independent TC oxidation under Ar atmosphere was only about  $0.173\text{ }\mu\text{mol}$ , indicating that the  $CO_2$  of TC mineralization was not completely converted into CO and  $CH_4$ . A similar phenomenon also occurred in the coupled reaction system using 50 mL of  $CO_2$  ( $2230\text{ }\mu\text{mol}$ ) as a reaction gas and 50 mL of  $20\text{ mg L}^{-1}$  TC ( $0.225\text{ }\mu\text{mol}$ ) as the reaction

solution. It can be seen from the coupled reaction system (Fig. 5e) that the amount of generated CO and  $CH_4$  was around  $1.3\text{ }\mu\text{mol}$ , in which about  $0.173\text{ }\mu\text{mol}$  of CO and  $CH_4$  stemmed from the TC decomposition, and approximately  $1.13\text{ }\mu\text{mol}$  of CO and  $CH_4$  came from the injected  $CO_2$ . It was clear that only 3.9% of  $CO_2$  of TC mineralization and 0.051% of injected  $CO_2$  were utilized to participate in photocatalytic  $CO_2$  reduction, which was consistent with the strong peaks of residual  $CO_2$  and  $^{13}CO_2$  in the following  $^{13}CO_2$  isotope labelling mass spectra at the wide  $m/z$  range from 14 to 46 (Fig. S8).

To further confirm that the produced CO and  $CH_4$  not only originated from  $CO_2$  reaction raw material, but also stemmed from part of  $CO_2$  of the TC decomposition. Thus, the  $^{13}CO_2$  isotope labelling experiment was carried out to track the carbon source in the coupled reaction system. As a reference, the resulting product using  $^{12}CO_2$  as substrate was also identified by GC-MS. The enlarged  $m/z$  region between 14 and 31 of mass spectrum was exhibited in Fig. 5f, only the two peaks at  $m/z = 16$  ( $^{12}CH_4$ ) and  $m/z = 28$  ( $^{12}CO$ ) in the mass spectrum could be observed



**Fig. 5.** Time courses of photocatalytic yields of CO (a) and CH<sub>4</sub> (b) for different times, and (c) the corresponding gas production rate of the as-obtained samples; (d) Photocatalytic activity of 70IB/CNx with different reaction conditions; (e) Effect of different reaction systems on 70IB/CNx; (f) GC-MS patterns of the produced CO and CH<sub>4</sub> over 70IB/CNx using  $^{12}\text{CO}_2$  and  $^{13}\text{CO}_2$  as the carbon source.

using  $^{12}\text{CO}_2$  as the carbon source. Once  $^{12}\text{CO}_2$  was replaced by  $^{13}\text{CO}_2$ , the  $^{13}\text{C}$  isotope labelling products of  $^{13}\text{CH}_4$  ( $m/z = 17$ ) and  $^{13}\text{CO}$  ( $m/z = 29$ ) were found, besides, some traces of  $^{12}\text{CH}_4$  ( $m/z = 16$ ) and  $^{12}\text{CO}$  ( $m/z = 28$ ) were also observed in the mass spectrum, illustrating that gases products were not only derived from  $\text{CO}_2$ , but also from traces of  $\text{CO}_2$  of TC mineralization. Soon afterwards, the liquid phase product using the  $\text{CO}_2$  and isotope  $^{13}\text{CO}_2$  as the reaction gas, respectively, was analyzed by LC-MS. It can be seen from the corresponding LC-MS spectra (Figs. S9 and 10), the intermediates of TC degradation using the isotope  $^{13}\text{CO}_2$  as the carbon source were basically similar to those of the  $\text{CO}_2$  as the reaction gas, further illustrating that  $\text{CO}_2$  only participated in the  $\text{CO}_2$  reduction rather than TC oxidation. Based on the LC-MS analysis (Fig. S11), the ion at  $m/z = 445$  was designated to initialized TC molecule [50]. Besides, the chief intermediates of TC degradation whose  $m/z$  situated at 461, 427, 432, 428, 417, 403, 340, 326, 279, 249, 171, 164.0, 154, 149, 118 and 114, corresponding to diverse structures [51–54]. Subsequently, the possible degradation routes of TC were exhibited in Fig. S12. During the photocatalytic reaction process, the intermediate C1 ( $m/z = 461$ ) and C5 ( $m/z = 427$ ) was the hydroxylated product through hydroxylation of TC molecule. Whereafter, the product C1 was converted to C2 ( $m/z = 432$ ) by loss of N-methyl group and dehydration, which further generated the C3 ( $m/z = 417$ ) via removal of N-methyl group. And then the C4 ( $m/z = 340$ ) was formed through

deamidation and dehydration of C3. Subsequently, C4 decomposed into C9 ( $m/z = 326$ ) via demethylation. Meanwhile, the C5 underwent deamidation reaction to generate C6 ( $m/z = 410$ ), and then transformed into C7 ( $m/z = 428$ ) by hydroxylation. Then, C8 ( $m/z = 403$ ) and C9 ( $m/z = 326$ ) was formed through successive ring opening, loss of the methyl and amino groups. Subsequently, the C9 decomposed into C10 ( $m/z = 279$ ) and further degraded into C11 ( $m/z = 249$ ) by ring-opening or loss of functional groups. Next, the C11 degraded separately into C12 ( $m/z = 171$ ) and C13 ( $m/z = 164$ ). Ultimately, some small intermediates, such as C14 ( $m/z = 154$ ), C15 ( $m/z = 149$ ), C16 ( $m/z = 118$ ), C17 ( $m/z = 114$ ) were produced under the attack of  $\bullet\text{OH}$  and  $\text{h}^+$ , which constantly degraded into even smaller organic molecules until further completely broken down into  $\text{CO}_2$  and  $\text{H}_2\text{O}$ . The above results showed that the coupled reaction system was a cyclic, green and efficient reaction system.

Besides, the other two pollutants, rhodamine B (RhB) and phenol, as common water contaminants, were utilized to investigate the impact of electron donating ability of contaminants on the synergic  $\text{CO}_2$  conversion. As displayed in Figs. S13a–c, the introduction of pollutants could heighten the reduction of  $\text{CO}_2$ . Interestingly, the higher the removal efficiency of TC was, the more favorable to the synergic  $\text{CO}_2$  conversion. The outcome could be due to different pollutant molecules with distinct electron donating capability in the coupled system. The above results



manifested that TC molecules as electron donors could distinctly enhance the synergistic CO<sub>2</sub> reduction because of TC molecules with higher electron-donating capacity.

In addition, the cycling stability of 70IB/CNx composite was assessed by recycling experiment of CO<sub>2</sub> reduction coupled with TC degradation. As presented in Fig. 6a, 70IB/CNx photocatalyst maintained a stable photocatalytic activity for CO<sub>2</sub> conversion and TC removal after five successive cycles, indicating that 70IB/CNx photocatalyst revealed good stability. Furthermore, the XRD profiles (Fig. 6b) of 70IB/CNx before and after reaction certified that the phase structure was well maintained.

Considering that the microstructure directly affects the number of active sites and the adsorption capacity of photocatalyst. Thus, N<sub>2</sub> adsorption-desorption tests of materials were implemented and revealed in Fig. 7a. It can be seen that the pure BiOBr, IB, CN, CNx and 70IB/CNx with type IV hysteresis loop implied the formation of mesoporous structures, which were in accord with the corresponding distribution curves of pore size (Fig. S14). The BET surface of 70IB/CNx heterojunction was obviously larger than that of the other photocatalysts, illustrating that 70IB/CNx with stronger adsorption property could provide more surface sites. As we all known that the specific surface area directly affects the photocatalytic properties of the photocatalyst. It is necessary to exclude the factor of specific surface area for exploring the main active centers of the enhanced photocatalytic properties. Thus, the surface area-normalized TC reaction rate ( $k_{TC}'$ ) and gases generation rate ( $k_{CO}'$  and  $k_{CH_4}'$ ) for the 70B/CNx, 70IB/CN and 70IB/CNx were discussed. And the corresponding BET, TC reaction rate ( $k_{TC}$ ), CO generation rate ( $k_{CO}$ ), CH<sub>4</sub> generation rate ( $k_{CH_4}$ ) were exhibited in Fig. S15a-d and summarized in Table S1 and Table S2. As presented in Table S1 and Table S2, a strong correlation existed between the  $k_{CO}'$ ,  $k_{CH_4}'$  and  $k_{TC}'$  for the as-obtained samples. It can be seen that the 70B/CNx and 70IB/CN presented similar  $k_{TC}'$  values, which were 0.019 and 0.020 h<sup>-1</sup>.m<sup>-2</sup>.g, respectively. Whereas, when the I<sup>-</sup> and N vacancy were introduced simultaneously, the  $k_{TC}'$  value of 70IB/CNx was increased by 0.018 h<sup>-1</sup>.m<sup>-2</sup>.g (48.6%) and 0.017 h<sup>-1</sup>.m<sup>-2</sup>.g (45.9%), respectively, in comparison with the 70B/CNx and 70IB/CN, indicating that the introduced I<sup>-</sup> as the main reactive center participated in TC oxidation. An opposite phenomenon appeared in the surface area-normalized gases generation rate, as compared to 70IB/CNx, the 70IB/CN and 70B/CNx exhibited much lower the  $k_{CO}'$  and  $k_{CH_4}'$  values were decreased from 0.147 to 0.108 μmol.h<sup>-1</sup>.m<sup>-2</sup> (26.5%) and 0.131 μmol.h<sup>-1</sup>.m<sup>-2</sup> (10.9%), respectively, illustrating that the introduced N vacancy as the major reactive center was involved in CO<sub>2</sub> reduction. The above results delineated that the I<sup>-</sup> acted as the main reactive center of oxidized half-reaction, whereas, N vacancy served as the main reactive center of the reduced semi-reaction in the coupled reaction system.

In order to verify the above conclusion, CO<sub>2</sub> adsorption isotherms (Fig. 7b) of the as-obtained samples were actualized. Similar to N<sub>2</sub> sorption isotherm, the 70IB/CNx presented largest adsorption capacity of CO<sub>2</sub>. Moreover, the adsorption energies ( $E_{ads}$ ) of CO<sub>2</sub> on the surface of

IB, CNx and IB or CNx sides of IB/CNx were evaluated by DFT calculation (Fig. 7c). The  $E_{ads}$  values were 0.26, -0.19, -0.06, -3.13 eV for IB, CNx and IB or CNx sides of IB/CNx, respectively. Obviously, the pure CNx presented more negative  $E_{ads}$  value than that of IB, illustrating that CO<sub>2</sub> molecules could be more conducive to adsorb on the CNx surface. Moreover, the  $E_{ads}$  of CNx side and IB side for IB/CNx were -3.13 eV and -0.06 eV, respectively, suggesting that CO<sub>2</sub> was easier to adsorb on the surface of CNx side rather than IB side of IB/CNx. The above results implied that the half-reaction of CO<sub>2</sub> reduction in the coupled reaction system was more likely to occur on the CNx surface.

To further explore the kinetic energy barrier of each step, the calculations of Gibbs free energies were conducted on IB/CNx and CNx (Fig. 8a-c). Based on the calculated results, formation of \*COOH intermediates were the rate-determining step for both of them, and IB/CNx had a lower energy barrier (0.27 eV) than that of CNx (1.05 eV). This was mainly attributed to the fact that the construction of heterojunctions could efficiently increase the charge-enriched reaction sites, thereby stabilizing the rate-limiting \*COOH intermediates. As presented in Fig. 8a, the desorption energy of CO molecules ( $\Delta G(*+CO)$ ) was slightly higher than the hydrogenation energy of \*CHO ( $\Delta G(*CHO)$ ). It revealed that \*CO molecules had a tendency to react with electron to produce CH<sub>4</sub>, which was in line with a certain amount of CH<sub>4</sub> generated on pure CNx. On the contrary, the \*CO molecules were more likely to liberate from the surface of IB/CNx as final product, instead of further reduction into \*CHO, because the  $\Delta G(*+CO)$  was apparently lower than  $\Delta G(*CHO)$  (Fig. 8b). The above results indicated a great potential for CO<sub>2</sub> conversion on CNx, and it could act as the reactive sites for the S-scheme IB/CNx heterojunction (Fig. 8c). As observed from the in-situ FT-IR spectra (Fig. 8d), the characteristic peak at 1557 cm<sup>-1</sup> was attributed to \*COOH symmetric and asymmetric bending vibration. Besides, the strong band at 1716 cm<sup>-1</sup> could be assigned to the stretching vibration of C=O, which came from the accumulation of CO [55–57]. In addition, as the increase of the exposure time, the signal for \*COOH gradually enhanced with no obvious position change, indicating that HCOOH as the pivotal intermediate participated in the photocatalytic CO<sub>2</sub> reduction. Moreover, the peaks of \*OCH<sub>2</sub> at 1342 cm<sup>-1</sup> and \*OCH<sub>3</sub> at 1287 cm<sup>-1</sup> associated with CH<sub>4</sub> production were weaker than those of \*COOH, which were consistent with their different product selectivity.

### 3.3. Verification of the S-scheme charge transfer

In-situ irradiated XPS, as a pivotal technique, was applied to investigate the valence state of elements and transfer direction of electrons. As depicted in Fig. S16, it can be found that I, Br, O, Bi as well as C, N could be detected in IB and CNx, respectively. As expected, the 70IB/CNx composite was comprised of not only I, Br, O and Bi belonging to IB but also C and N pertaining to CNx, which revealed the hybridization of IB and CNx in the 70IB/CNx heterojunction. The detailed high-

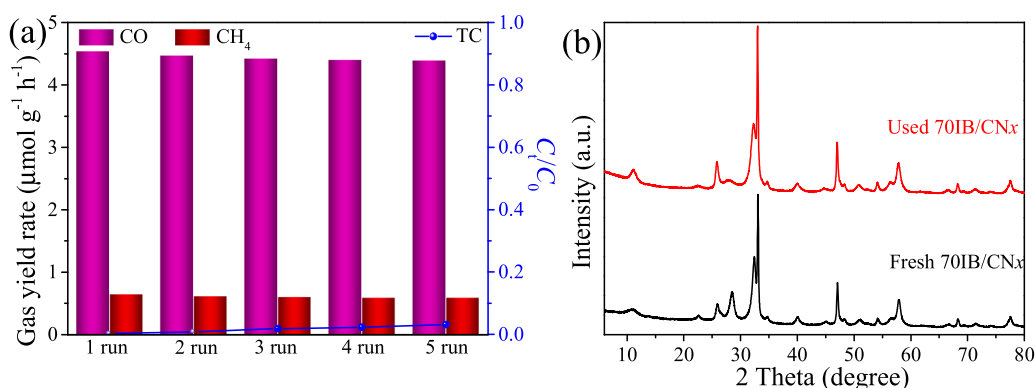
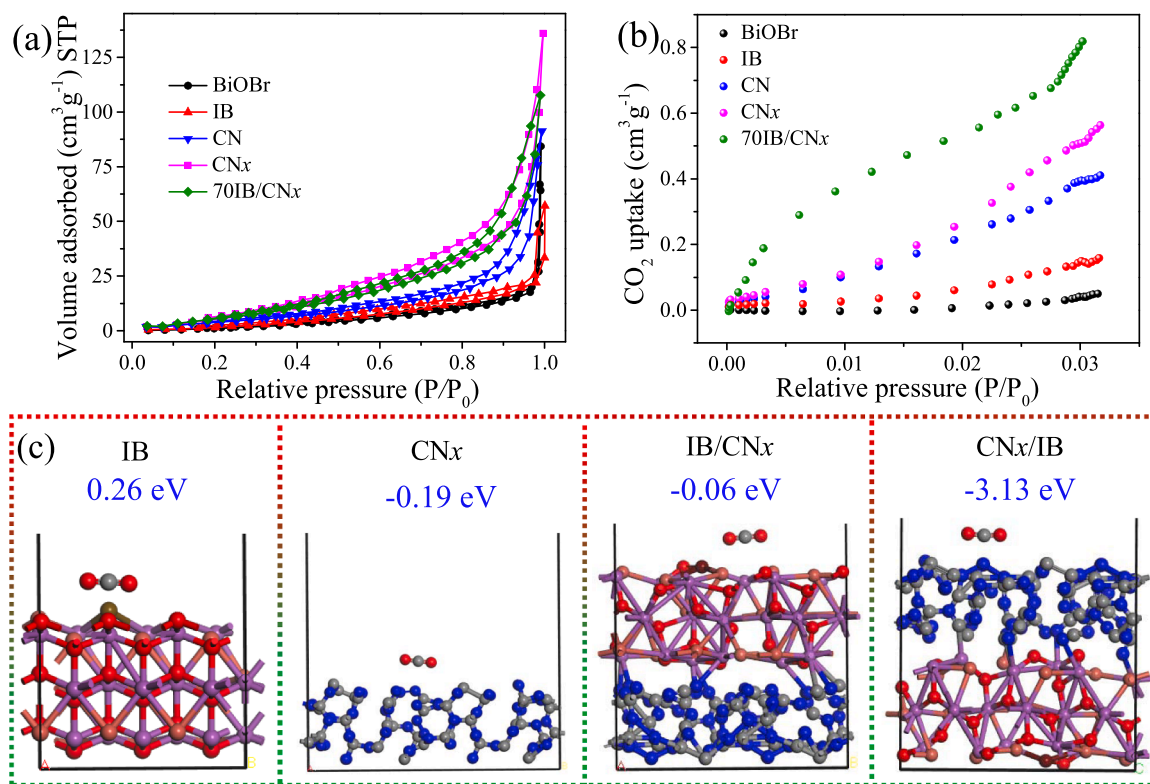
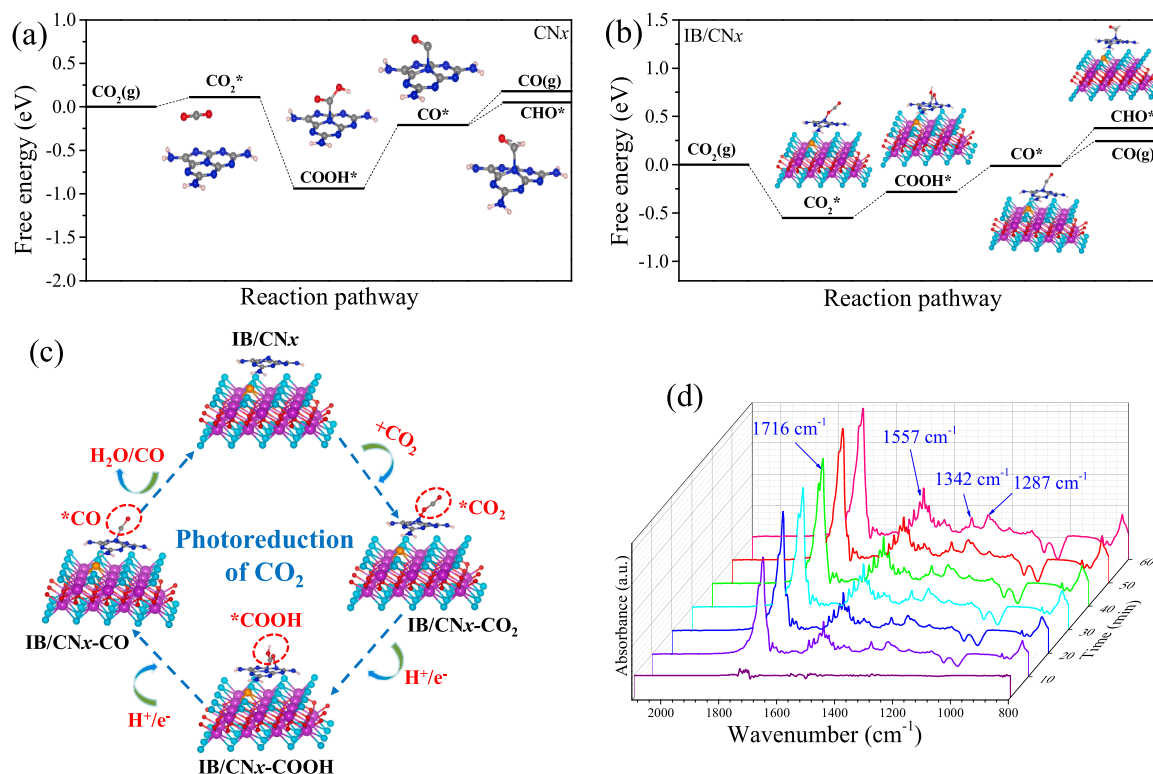


Fig. 6. (a) Cycling runs of 70IB/CNx for CO<sub>2</sub> reduction coupled with TC oxidation, and (b) XRD patterns of 70IB/CNx before and after used.



**Fig. 7.** (a) N<sub>2</sub> adsorption-desorption isotherms and (b) CO<sub>2</sub> adsorption isotherm of the as-obtained samples; (c) Optimized geometry structures and CO<sub>2</sub> adsorption energies on IB, CN<sub>x</sub>, IB/CNx and CN<sub>x</sub>/IB.



**Fig. 8.** Free energy diagrams of CN<sub>x</sub> (a) and IB/CNx (b) during CO<sub>2</sub> reduction; (c) The proposed reaction pathway of CO<sub>2</sub> to CO on IB/CNx; (d) In situ FTIR spectra of photocatalytic CO<sub>2</sub> reduction over 70IB/CNx at different time.

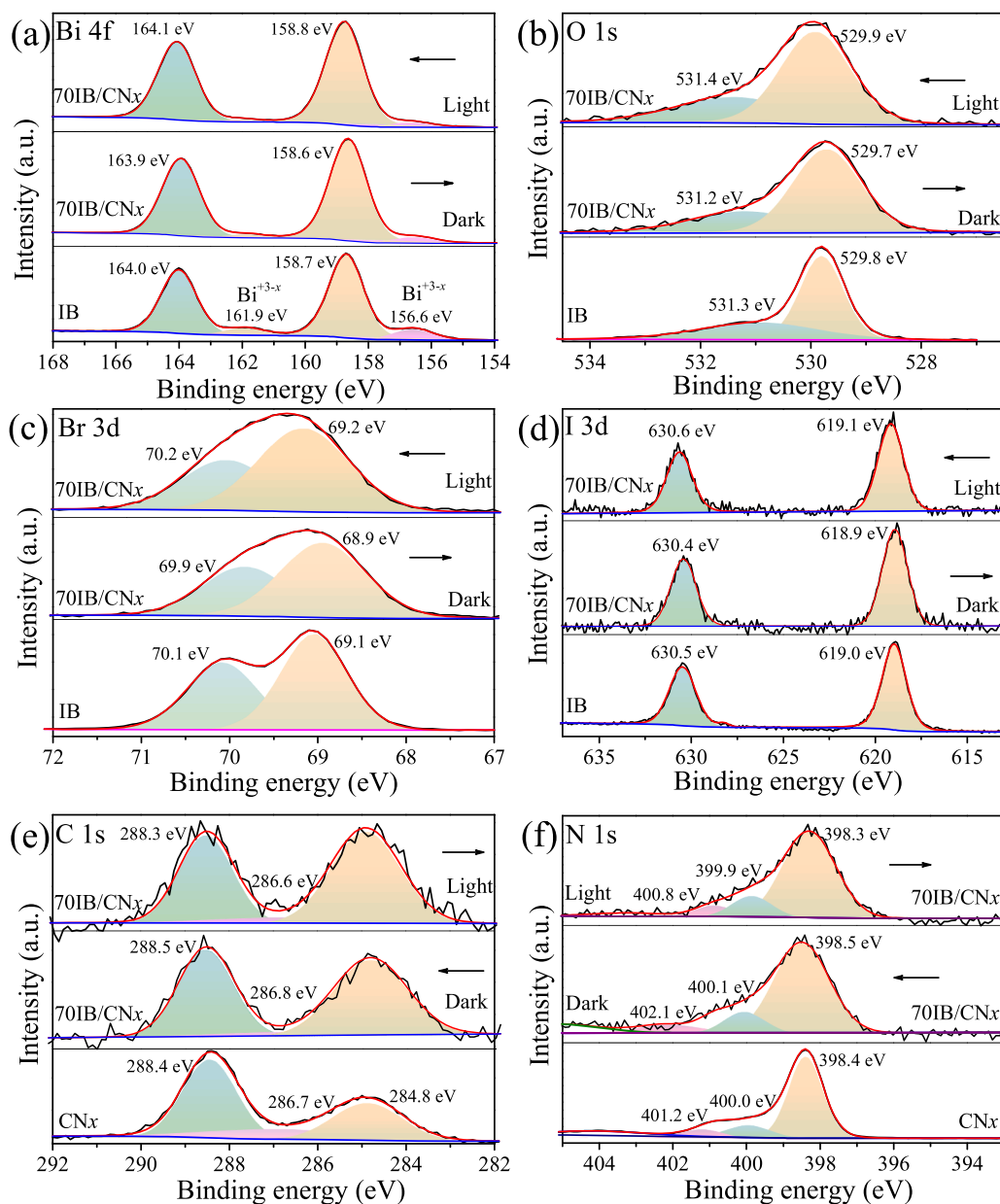


**Fig. 9.** In-situ XPS (a) Bi 4f, (b) O 1s, (c) Br 3d, (d) I 3d, (e) C 1s and (f) N 1s spectra of the prepared samples with and without illumination.

resolution spectra of Bi 4f, O 1s, Br 3d, I 3d, C 1s and N 1s were presented in Fig. 9a-f. For pristine IB, the binding energies (BEs) at 158.7 eV and 164.0 eV belonged to Bi 4f<sub>7/2</sub> and Bi 4f<sub>5/2</sub> of Bi<sup>3+</sup>, respectively (Fig. 9a). Besides, two weak peaks located at 156.6 and 161.9 eV, which matched with Bi 4f<sub>7/2</sub> and Bi 4f<sub>5/2</sub> of lower-valence Bi<sup>+3-x</sup> [16]. After coupling with CNx, the BEs of Bi 4f for 70IB/CNx composite shifted to lower BEs before illumination and higher BEs after illumination, verifying that the Bi specie of IB in 70IB/CNx heterojunction was electron acceptor in the dark but electron donor in the light. Besides, the O 1s of pure IB positioned at 529.8 eV and 531.3 eV assigned to Bi-O and hydroxyl, respectively (Fig. 9b). Compared to IB, the O 1s peaks of 70IB/CNx composite shifted to lower BEs without illumination and higher BEs within illumination. A similar phenomenon emerged in the Br 3d and I 3d spectra (Fig. 9c and d), the peaks of Br 3d and I 3d for 70IB/CNx heterojunction displayed more positive shift exposed to light and more negative shift prior to illumination than those of bare IB, revealing that Br and I element served as electron donor in the light but electron acceptor in the dark. Conversely, the BEs of C 1s (Fig. 9e) and N 1s (Fig. 9f) spectra in 70IB/CNx composite displayed a

slight negative shift under illumination and positive shift in darkness relative to pristine CNx, implying that the function of CNx was electron acceptor exposed to light but electron donor prior to illumination. This conclusion demonstrated that the e<sup>-</sup> transferred from CNx to IB without illumination but IB to CNx within illumination, indicating that the electrons migration route abided by S-scheme transfer path.

Soon afterwards, the work functions of IB and CNx were calculated to deeply inquire into the direction of electron migration between IB and CNx semiconductor. As delineated in Fig. 10a and b, the work functions of IB (102) and CNx (002) face were 5.34 and 6.89 eV, respectively, affirming that IB had a lower Fermi energy ( $E_F$ ) than that of CNx before contact (Fig. 10c). After close contact in the dark, the electron of CNx spontaneously shifted to IB through the interface until their  $E_F$  achieved balance. Subsequently, the interface region nearby CNx component accumulated positive charges due to lost electrons, resulting in the upward bending of band edge of CNx. Instead, the interface region around IB component had negative charges because of obtained electrons, leading to the downward bending of band edge of IB (Fig. 10d). Meanwhile, an internal electric field (IEF) was built at interface of IB/CNx

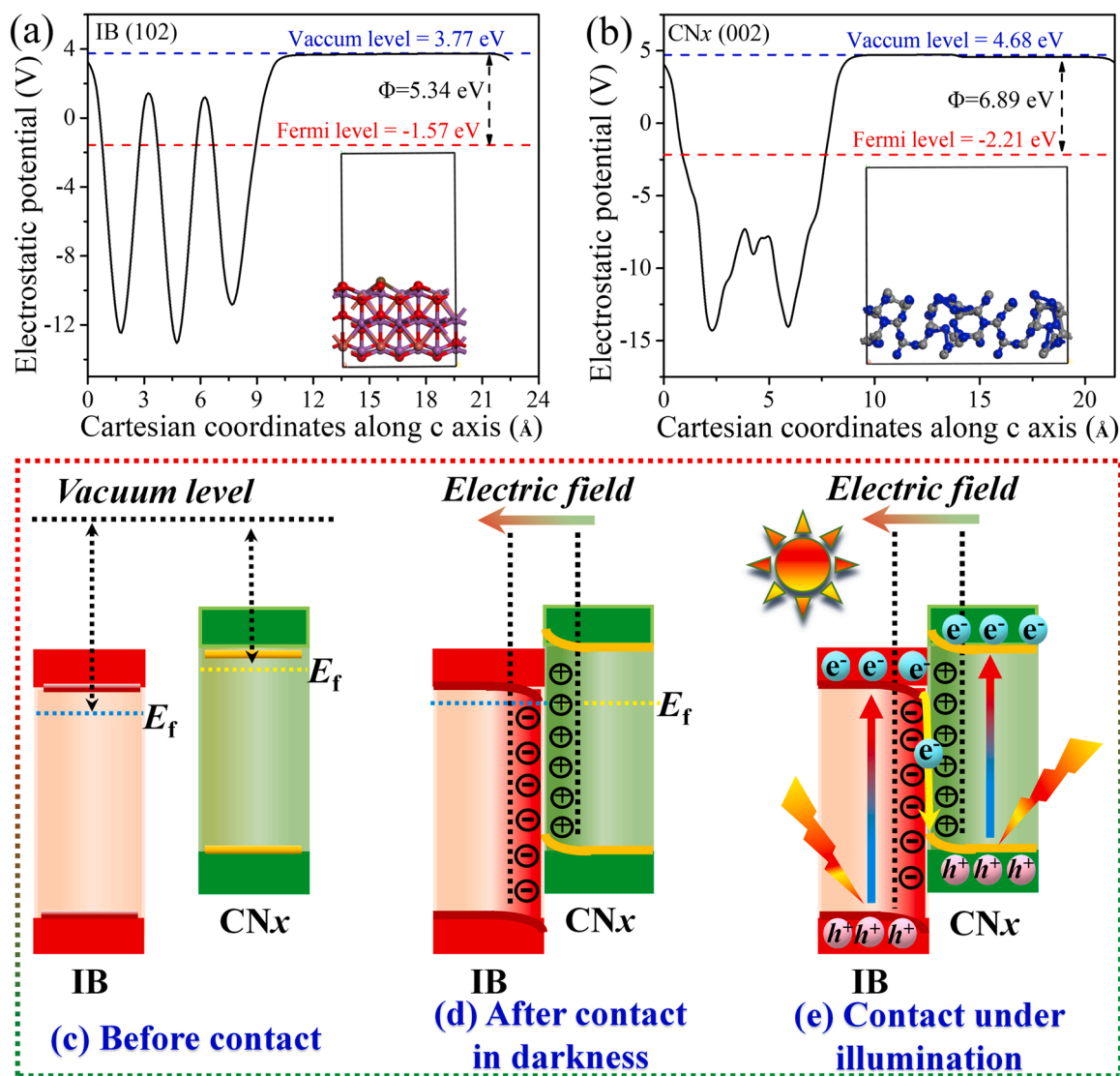


**Fig. 10.** The work function of (a) IB and (b) CNx; The diagram of electron migration between IB and CNx semiconductor (c) before and (d) after contacted in the dark, and (e) photo-induced carriers transfer mechanism in the IB/CNx photocatalyst exposed to light.

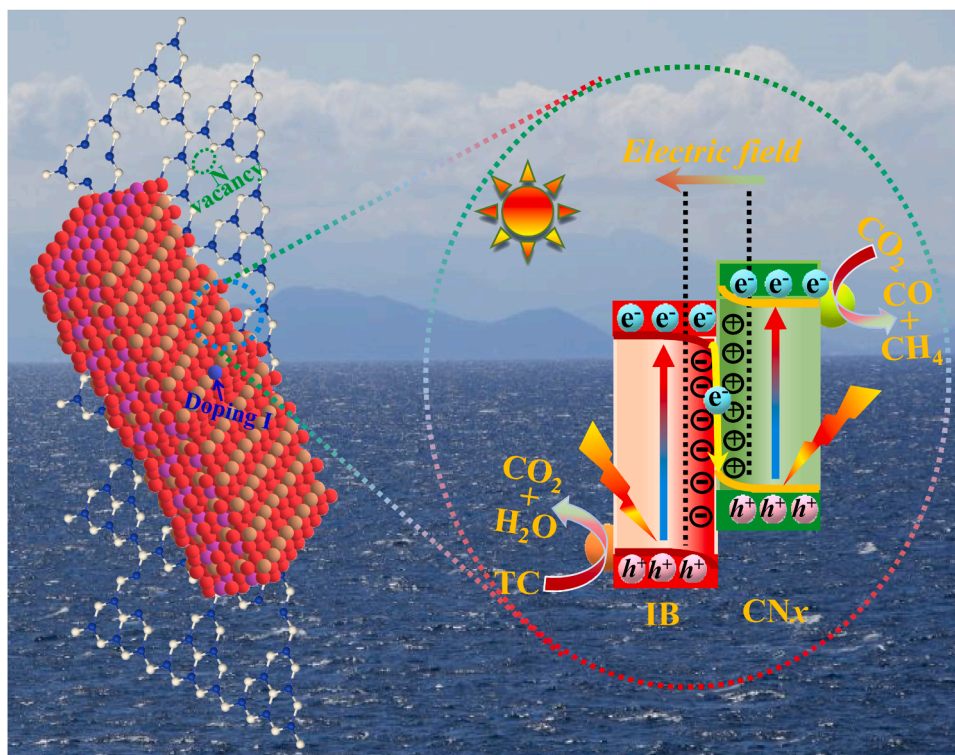
heterojunction, which could maintain the successive shift of electrons from CNx to IB. Once exposed to light, the IB and CNx were photoexcited to create the photogenerated electrons and holes. Subsequently, the photo-excited electrons could move in the opposite direction from IB to CNx, leading to the S-scheme transfer channel of electrons (Fig. 10e).

To provide more evidence of the S-scheme charge transfer in IB/CNx hybrid, the primary reactive species were probed by ESR measurements. Hereon, the superoxide radicals ( $\bullet\text{O}_2^-$ ) and hydroxyl radicals ( $\bullet\text{OH}$ ) was trapped by using 5,5-Dimethyl-1-pyrroline N-oxide (DMPO), producing the adducts of DMPO- $\bullet\text{O}_2^-$  and DMPO- $\bullet\text{OH}$ , respectively [58]. As presented in Fig. S17, for bare IB, the obvious EPR signal of DMPO- $\bullet\text{OH}$  was discovered, whereas hardly any EPR signal of DMPO- $\bullet\text{O}_2^-$  was observed, demonstrating that the IB promoted the generation of  $\bullet\text{OH}$  instead of  $\bullet\text{O}_2^-$ . Because the  $E_{\text{VB}}$  (2.02 V vs NHE) of pristine IB was much more positive than the potential of  $\text{OH}^-/\bullet\text{OH}$  (1.99 V vs NHE), whereas its  $E_{\text{CB}}$  (-0.20 V vs NHE) was less negative than the potential of  $\text{O}_2/\bullet\text{O}_2^-$  (-0.33 V vs NHE), which was not strong enough reduction capacity to reduce  $\text{O}_2$  into  $\bullet\text{O}_2^-$  [16]. On the contrary, the EPR signal of DMPO- $\bullet\text{O}_2^-$  was obviously detected but the signal of DMPO- $\bullet\text{OH}$  was hardly observed in the pure CNx. This result revealed that the CNx was favorable for engendering  $\bullet\text{O}_2^-$  rather than  $\bullet\text{OH}$ , which was attributed to its stronger reduction potential (-0.78 V vs NHE) than the potential of

$\text{O}_2/\bullet\text{O}_2^-$  (-0.33 V vs NHE) and the weaker oxidation potential (1.55 V vs NHE) than the potential of  $\text{OH}^-/\bullet\text{OH}$  (1.99 V vs NHE). More importantly, compared with pristine IB and CNx, the both DMPO- $\bullet\text{O}_2^-$  and DMPO- $\bullet\text{OH}$  EPR signals of 70IB/CNx were greatly facilitated, certifying that the construction of 70IB/CNx heterojunction could effectively accelerate the separation of carriers and thus generated more reactive free radicals. The above conclusions revealed the space distribution of reduction sites (CNx component) and oxidation sites (IB component) in the 70IB/CNx heterojunction by an S-scheme charges migration route and enormously boosting the  $\text{CO}_2$  reduction coupled with TC oxidation under illumination.

On the basis of the above-mentioned discussion, a feasible reaction mechanism over IB/CNx heterojunction was proposed and displayed in Scheme 2. Upon photoexcitation, the IB and CNx were photoexcited to produce the photo-induced electrons and holes. Soon afterwards, the carriers transferred via an S-scheme charges migration channel to drive the catalytic redox reaction. In other words, the correspondingly useless electrons on CB of IB recombined with futile holes on VB of CNx, meanwhile, persisting the electrons with strong reduction capacity on the CB of CNx and the holes with high oxidation ability on the VB of IB. Whereafter, the electrons with strong reduction capability on the CB of CNx could reduce  $\text{CO}_2$  to generate CO and  $\text{CH}_4$ , meantime, the  $\text{h}^+$  or





**Scheme 2.** Diagrammatic sketch for photocatalytic mechanism of IB/CNx heterojunction.

•OH with high oxidative potential on the VB of IB could participate in TC degradation, thereby, realizing the photocatalytic  $\text{CO}_2$  reduction synergistic TC degradation. This work further revealed that the introduction of double defects into S-scheme photocatalyst with strong driving force to achieve the simultaneous photo-redox reactions.

To investigate the separation rate of charges, the photoelectrochemical characterizations were carried out. Fig. 11a presented

the transient photocurrent curves (TPC) of the as-fabricated catalysts by turning on/off the irradiation light. Both BiOBr and CN exhibited low photocurrent density because of the poor separation of electron-hole pairs. After introducing defects into both of them, the photocurrent intensities of IB and CNx significantly enhanced in comparison with those of BiOBr and CN, affirming that the introducing defects were benefit to the separation of carriers. After hybridization of IB and CNx, the 70IB/

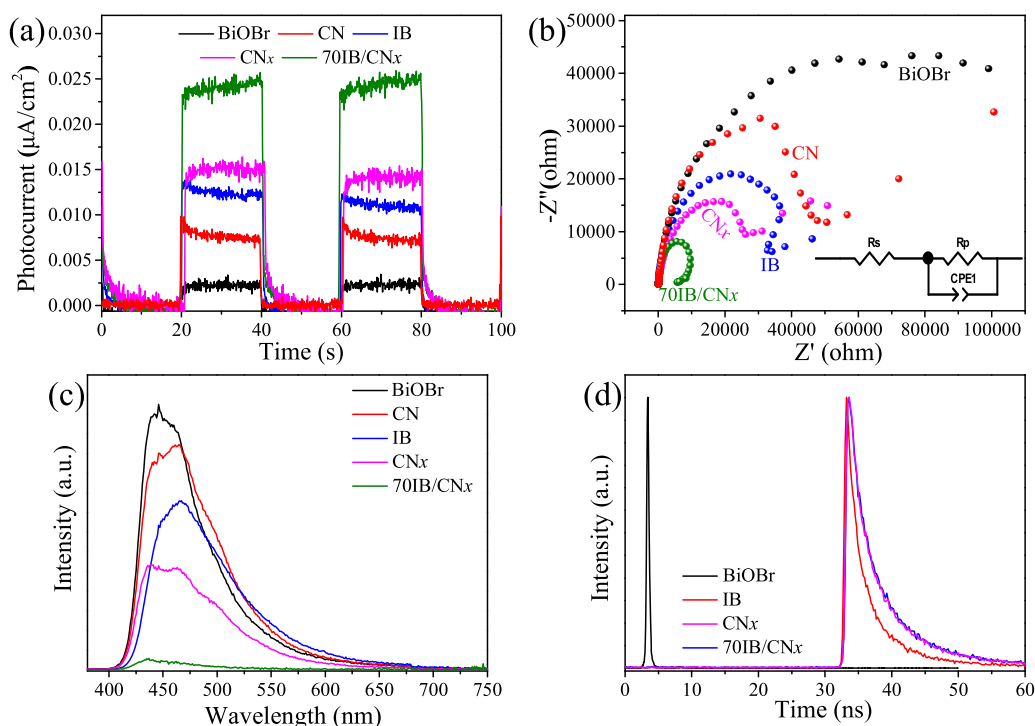


**Fig. 11.** (a) Photocurrent densities, (b) EIS curves, (c) PL spectra, and (d) TRPL decay curves of the as-prepared samples.

CNx heterojunction revealed apparently advanced photocurrent, indicating that the construction of S-scheme heterojunction effectively improved the separation of charges.

To further elucidate the charge electron transfer resistance, the EIS spectra were employed in darkness. Popularly, the smaller semicircle arc of EIS curves represented the lower interfacial transfer resistance of charges. As delineated in Fig. 11b, 70IB/CNx hybrid possessed the smaller arc radius than that of single components, implying that the synergistic effect of I doped and N defect could greatly reduce the interface migration resistance, thereby expediting the transfer and separation of carriers. In order to acquire the quantitative result, the fitted values of impedance were presented in Table S3, and the corresponding simulated equivalent circuit was inserted in Fig. 11b. The fitted  $R_s$  values represented the ohmic resistance between the material and the electrode, and the  $R_p$  was the transfer resistance of photogenerated carriers in material. As can be seen from the fitted  $R_s$  values, the  $R_s$  values for diverse materials with small gaps demonstrated the close ohmic resistance for all samples. On the contrary, the  $R_p$  values for BiOBr, CN, IB, CNx, and 70IB/CNx photocatalysts presented enormous variations, which were  $5.31 \times 10^{12}$ ,  $1.14 \times 10^5$ ,  $4.59 \times 10^4$ ,  $4.16 \times 10^4$ , and  $3.31 \times 10^4 \Omega$ , respectively. Apparently, the 70IB/CNx possessed the smallest  $R_p$  values, illustrating that the 70IB/CNx heterojunction had a highest kinetic barrier.

To better research the recombination rate of electron and hole, the PL spectra were measured and delineated in Fig. 11c. The bare BiOBr revealed a strong PL signal, but once  $I^-$  was introduced, the PL intensity decreased significantly, illustrating that the I doped could availably decrease the recombination rate of charges. A similar phenomenon occurred in CNx, after the introduction of N defect, the PL intensity was lower than that of CN. Upon the combination of IB and CNx, 70IB/CNx presented the weakest PL intensity, demonstrated that the synergistic effect of the introduced double defects and the S-scheme heterojunction could high-efficiently suppress the recombination of carriers. Immediately, the decay lifetimes of carriers were further revealed by the TRPL decay curves (Fig. 11d), and the corresponding parameters were summarized in Table S4. The 70IB/CNx displayed much longer average lifetime than that of BiOBr, IB and CNx, verifying that the extended lifetime of carriers in the 70IB/CNx heterojunction. The above results indicated that the simultaneous introduction of both N vacancy and I induced Br vacancy into the S-scheme heterojunction not only promoted separation of charges and extended lifetime of carriers, but also offered more reaction sites for participating in chemical reaction and thence advanced photocatalytic activity toward  $CO_2$  reduction coupled with TC oxidation.

## 4. Conclusions

In summary, a dual defective I doped BiOBr/N vacancy g-C<sub>3</sub>N<sub>4</sub> heterojunction was designed and applied to the coupled reaction system of  $CO_2$  reduction integrated with wastewater purification. The synergistic effect of double defects not only offered more reaction sites for  $CO_2$  conversion, but also enhanced the oxidation ability for pollutants removal. Besides, substantial defects as charge acceptors could enhance the transfer efficiency of carriers, meanwhile, the coupled reaction system realized the full utilization of the charges, thereby, improving the utilization rate of carriers and the photocatalytic activity. Moreover, the coinstantaneous introduction of dual defects into heterojunction could supplied a doable tactic to capacitate dual-functional photocatalyst for promising multi-applications in renewable energy generation and environmental remediation.

## CRediT authorship contribution statement

**Xuemei Jia:** Validation, investigation, Writing – review & editing, Funding acquisition. **Cheng Hu:** Formal analysis, investigation. **Haoyu Sun:** Formal analysis, Validation. **Jing Cao:** Writing – review & editing,

Funding acquisition. **Haili Lin:** Project administration, Funding acquisition. **Xinyue Li:** Validation, investigation. **Shifu Chen:** Conceptualization, Funding acquisition.

## Declaration of Competing Interest

The authors declare that they have no known competing financial interests or personal relationships that could have appeared to influence the work reported in this paper.

## Data Availability

No data was used for the research described in the article.

## Acknowledgements

This work was financially supported by the National Natural Science Foundation of China (22202077, 21902056, 51972134, 51772118), the University Natural Science Research Project of Anhui Province (KJ2021A0522, KJ2020ZD007, gxbjZD2021096), and the Anhui Provincial Natural Science Foundation (1908085MB36).

## Appendix A. Supporting information

Supplementary data associated with this article can be found in the online version at doi:10.1016/j.apcatb.2022.122232.

## References

- [1] A. Meng, B. Cheng, H. Tan, J. Fan, C. Su, J. Yu, TiO<sub>2</sub>/polydopamine S-scheme heterojunction photocatalyst with enhanced CO<sub>2</sub>-reduction selectivity, *Appl. Catal. B: Environ.* 289 (2021), 120039.
- [2] L. Yuan, K.Q. Lu, F. Zhang, X. Fu, Y.J. Xu, Unveiling the interplay between light driven CO<sub>2</sub> photocatalytic reduction and carbonaceous residues decomposition: a case study of Bi<sub>2</sub>WO<sub>6</sub>-TiO<sub>2</sub> binanosheets, *Appl. Catal. B: Environ.* 237 (2018) 424–431.
- [3] X. Hu, Z. Xie, Q. Tang, H. Wang, L. Zhang, J. Wang, Enhanced CH<sub>4</sub> yields by interfacial heating-induced hot water steam during photocatalytic CO<sub>2</sub> reduction, *Appl. Catal. B: Environ.* 298 (2021), 120635.
- [4] K.Q. Lu, Y.H. Li, F. Zhang, M.Y. Qi, X. Chen, Z.R. Tang, Y.M.A. Yamada, M. Anpo, M. Conte, Y.J. Xu, Rationally designed transition metal hydroxide nanosheet arrays on graphene for artificial CO<sub>2</sub> reduction, *Nat. Commun.* 11 (2020) 5181.
- [5] S. Wang, X. Han, Y. Zhang, N. Tian, T. Ma, H. Huang, Inside-and-out semiconductor engineering for CO<sub>2</sub> photoreduction: From recent advances to new trends, *Small Struct.* 2 (2021) 2000061.
- [6] X. Liu, S. Inagaki, J. Gong, Heterogeneous molecular systems for photocatalytic CO<sub>2</sub> reduction with water oxidation, *Angew. Chem. Int. Ed.* 55 (2016) 14924–14950.
- [7] J. Song, Y. Lu, Y. Lin, Q. Liu, X. Wang, W. Su, A direct Z-scheme alpha-Fe<sub>2</sub>O<sub>3</sub>/LaTiO<sub>2</sub>N visible-light photocatalyst for enhanced CO<sub>2</sub> reduction activity, *Appl. Catal. B: Environ.* 292 (2021), 120185.
- [8] C. Han, Y.H. Li, J.Y. Li, M.Y. Qi, Z.R. Tang, Y.J. Xu, Cooperative syngas production and C-N bond formation in one photoredox cycle, *Angew. Chem. Int. Ed.* 60 (2021) 7962–7970.
- [9] L. Yuan, M.Y. Qi, Z.R. Tang, Y.J. Xu, Coupling strategy for CO<sub>2</sub> valorization integrated with organic synthesis by heterogeneous photocatalysis, *Angew. Chem. Int. Ed.* 60 (2021) 21150–21172.
- [10] M.Y. Qi, M. Conte, M. Anpo, Z.R. Tang, Y.J. Xu, Cooperative coupling of oxidative organic synthesis and hydrogen production over semiconductor-based photocatalysts, *Chem. Rev.* 121 (2021) 13051–13085.
- [11] G.X. Dong, W. Zhang, Y.F. Mu, K. Su, M. Zhang, T.B. Lu, A halide perovskite as a catalyst to simultaneously achieve efficient photocatalytic CO<sub>2</sub> reduction and methanol oxidation, *Chem. Commun.* 56 (2020) 4664–4667.
- [12] L. Wang, X. Zhang, L. Yang, C. Wang, H. Wang, Photocatalytic reduction of CO<sub>2</sub> coupled with selective alcohol oxidation under ambient conditions, *Catal. Sci. Technol.* 5 (2015) 4800–4805.
- [13] Y. Chen, M. Wang, Y. Ma, Y. Li, J. Cai, Z. Li, Coupling photocatalytic CO<sub>2</sub> reduction with benzyl alcohol oxidation to produce benzyl acetate over Cu<sub>2</sub>O/Cu, *Catal. Sci. Technol.* 8 (2018) 2218–2223.
- [14] H. Huang, J. Zhao, Y. Du, C. Zhou, M. Zhang, Z. Wang, Y. Weng, J. Long, J. Hofkens, J.A. Steele, M.B.J. Roeffaers, Direct Z-scheme heterojunction of semicoherent FAPbBr<sub>3</sub>/Bi<sub>2</sub>WO<sub>6</sub> interface for photoredox reaction with large driving force, *ACS Nano* 14 (2020) 16689–16697.
- [15] H. Wang, D. Yong, S. Chen, S. Jiang, X. Zhang, W. Shao, Q. Zhang, W. Yan, B. Pan, Y. Xie, Oxygen-vacancy-mediated exciton dissociation in BiOBr for boosting charge-carrier-involved molecular oxygen activation, *J. Am. Chem. Soc.* 140 (2018) 1760–1766.

- [16] X.M. Jia, Q.F. Han, H.Z. Liu, S.Z. Li, H.P. Bi, A dual strategy to construct flowerlike S-scheme BiOBr/BiOAc<sub>1-x</sub>Br<sub>x</sub> heterojunction with enhanced visible-light photocatalytic activity, *Chem. Eng. J.* 399 (2020), 125701.
- [17] X.B. Li, J. Xiong, X.M. Gao, J. Ma, Z. Chen, B.B. Kang, J.Y. Liu, H. Li, Z.J. Feng, J. T. Huang, Novel BP/BiOBr S-scheme nano-heterojunction for enhanced visible-light photocatalytic tetracycline removal and oxygen evolution activity, *J. Hazard. Mater.* 387 (2020), 121690.
- [18] H.L. Lin, X. Li, J. Cao, S.F. Chen, Y. Chen, Novel I-doped BiOBr composites: modulated valence bands and largely enhanced visible light photocatalytic activities, *Catal. Commun.* 49 (2014) 87–91.
- [19] C.J. Bi, J. Cao, H.L. Lin, Y.J. Wang, S.F. Chen, Tunable photocatalytic and photoelectric properties of I-doped BiOBr photocatalyst: Dramatic pH effect, *RSC Adv.* 6 (2016) 15525–15534.
- [20] L.F. Qi, Y.W. Yang, P.X. Zhang, Y. Le, C. Wang, T. Wu, Hierarchical flower-like BiOI<sub>1-x</sub>Br<sub>x</sub> solid solution spheres with enhanced visible-light photocatalytic activity, *Appl. Surf. Sci.* 467–468 (2019) 792–801.
- [21] Y. Bai, X. Shi, P.Q. Wang, L. Wang, H.Q. Xie, Z.J. Li, L.B. Qu, L.Q. Ye, Synthesis of one-dimensional Bi<sub>5</sub>O<sub>7</sub>Br<sub>0.5</sub> solid solution for effective real oilfield wastewater treatment via exciton photocatalytic process, *J. Taiwan. Inst. Chem. E* 91 (2018) 358–368.
- [22] W.J. Kim, D. Pradhan, B.K. Min, Y. Sohn, Adsorption/photocatalytic activity and fundamental natures of BiOCl and BiOCl<sub>1-x</sub>I<sub>x</sub> prepared in water and ethylene glycol environments, and Ag and Au-doping effects, *Appl. Catal. B: Environ.* 147 (2014) 711–725.
- [23] G.G. Liu, T. Wang, S.X. Ouyang, L.Q. Liu, H.Y. Jiang, Q. Yu, T. Kako, J.H. Ye, Band-structure-controlled BiO(ClBr)<sub>(1-x)/2</sub>I<sub>x/2</sub> solid solutions for visible-light photocatalysis, *J. Mater. Chem. A* 3 (2015) 8123–8132.
- [24] J. Fu, Q. Xu, J. Low, C. Jiang, J. Yu, Ultrathin 2D/2D WO<sub>3</sub>/g-C<sub>3</sub>N<sub>4</sub> step-scheme H<sub>2</sub>-production photocatalyst, *Appl. Catal. B: Environ.* 243 (2019) 556–565.
- [25] X. Chen, R.T. Guo, W.G. Pan, Y. Yuan, X. Hu, Z.X. Bi, J. Wang, A novel double S-scheme photocatalyst Bi<sub>7</sub>O<sub>9</sub>I<sub>3</sub>/Cd<sub>0.5</sub>Zn<sub>0.5</sub>SQDs/WO<sub>3-x</sub> with efficient full-spectrum-induced phenol photodegradation, *Appl. Catal. B: Environ.* 318 (2022), 121839.
- [26] F.A. Qaraah, S.A. Mahyoub, A. Hezam, A. Qaraah, F. Xin, G.L. Xiu, Synergistic effect of hierarchical structure and S-scheme heterojunction over O-doped g-C<sub>3</sub>N<sub>4</sub>/N-doped Nb<sub>2</sub>O<sub>5</sub> for highly efficient photocatalytic CO<sub>2</sub> reduction, *Appl. Catal. B: Environ.* 315 (2022), 121585.
- [27] Y. Wang, Y.R. Tang, J.H. Sun, X. Wu, H. Liang, Y. Qu, L.Q. Jing, BiFeO<sub>3</sub>/Bi<sub>2</sub>Fe<sub>4</sub>O<sub>9</sub> S-scheme heterojunction hollow nanospheres for high-efficiency photocatalytic o-chlorophenol degradation, *Appl. Catal. B: Environ.* 319 (2022), 121893.
- [28] Y. Li, F. Gong, Q. Zhou, X.H. Feng, J.J. Fan, Q.J. Xiang, Crystalline isotype heptazine/triazine-based carbon nitride heterojunctions for an improved hydrogen evolution, *Appl. Catal. B: Environ.* 268 (2020), 118381.
- [29] G. Zhou, Y. Shan, Y.Y. Hu, X.Y. Xu, L.Y. Long, J.L. Zhang, J. Dai, J.H. Guo, J. C. Shen, S. Li, L.Z. Liu, X.L. Wu, Half-metallic carbon nitride nanosheets with microgrid mode resonance structure for efficient photocatalytic hydrogen evolution, *Nat. Commun.* 9 (2018) 3366.
- [30] M.F. Liang, T. Borjigin, Y.H. Zhang, H. Liu, B.H. Liu, H. Guo, Z-scheme Au@Void/g-C<sub>3</sub>N<sub>4</sub>/SnS yolk-shell heterostructures for superior photocatalytic CO<sub>2</sub> reduction under visible light, *ACS Appl. Mater. Interfaces* 10 (2018) 34123–34131.
- [31] Q.X. Liu, L.H. Ai, J. Jiang, MXene-derived TiO<sub>2</sub>@C/g-C<sub>3</sub>N<sub>4</sub> heterojunctions for highly efficient nitrogen photofixation, *J. Mater. Chem. A* 6 (2018) 4102–4110.
- [32] Y. Shen, Q.T. Han, J.Q. Hu, W. Gao, L. Wang, L.Q. Yang, C. Gao, Q. Shen, C.P. Wu, X.Y. Wang, X. Zhou, Y. Zhou, Z.G. Zou, Artificial trees for artificial photosynthesis: Construction of dendrite-structured α-Fe<sub>2</sub>O<sub>3</sub>/g-C<sub>3</sub>N<sub>4</sub> Z-scheme system for efficient CO<sub>2</sub> reduction into solar fuels, *ACS Appl. Energy Mater.* 3 (2020) 6561–6572.
- [33] H. Yu, R. Shi, Y. Zhao, T. Bian, Y. Zhao, C. Zhou, G.I.N. Waterhouse, L.Z. Wu, C. H. Tung, T. Zhang, Alkali-assisted synthesis of nitrogen deficient graphitic carbon nitride with tunable band structures for efficient visible-light-driven hydrogen evolution, *Adv. Mater.* 29 (2017) 1605148.
- [34] D. Ruan, S. Kim, M. Fujitsuka, T. Majima, Defects rich g-C<sub>3</sub>N<sub>4</sub> with mesoporous structure for efficient photocatalytic H<sub>2</sub> production under visible light irradiation, *Appl. Catal. B: Environ.* 238 (2018) 638–646.
- [35] Q. Tay, P. Kanhere, C.F. Ng, S. Chen, S. Chakraborty, A.C.H. Huan, T.C. Sum, R. Ahuja, Z. Chen, Defect engineered g-C<sub>3</sub>N<sub>4</sub> for efficient visible light photocatalytic hydrogen production, *Chem. Mater.* 27 (2015) 4930–4933.
- [36] S.Q. Sun, Y.C. Wu, J.F. Zhu, C.J. Lu, Y. Sun, Z. Wang, J. Chen, Stabilizing plasma-induced highly nitrogen-deficient g-C<sub>3</sub>N<sub>4</sub> by heteroatom-refilling for excellent lithium-ion battery anodes, *Chem. Eng. J.* 427 (2022), 131032.
- [37] Y. Bai, L.Q. Ye, T. Chen, P.Q. Wang, L. Wang, X. Shi, P.K. Wong, Synthesis of hierarchical bismuth-rich Bi<sub>4</sub>O<sub>3</sub>Br<sub>1-2x</sub> solid solutions for enhanced photocatalytic activities of CO<sub>2</sub> conversion and Cr(VI) reduction under visible light, *Appl. Catal. B: Environ.* 203 (2017) 633–640.
- [38] J.J. Wu, L.J. Xiong, Y.J. Hu, Y. Yang, X.Y. Zhang, T.Y. Wang, Z. Tang, A.W. Sun, Y. Zhou, J.Y. Shen, Z.G. Zou, Organic half-metal derived erythroid-like BiVO<sub>4</sub>/hm-C<sub>6</sub>N<sub>3</sub> Z-scheme photocatalyst: reduction sites upgrading and rate-determining step modulation for overall CO<sub>2</sub> and H<sub>2</sub>O conversion, *Appl. Catal. B: Environ.* 295 (2021), 120277.
- [39] G. Kresse, J. Furthmüller, Efficient iterative schemes for ab initio total-energy calculations using a plane-wave basis set, *Phys. Rev. B* 54 (1996) 11169–11186.
- [40] G. Kresse, D. Joubert, From ultrasoft pseudopotentials to the projector augmented-wave method, *Phys. Rev. B* 59 (1999) 1758.
- [41] J.P. Perdew, J.A. Chevary, S.H. Vosko, K.A. Jackson, M.R. Pederson, D.J. Singh, C. Fiolhais, Atoms, molecules, solids, and surfaces: applications of the generalized gradient approximation for exchange and correlation, *Phys. Rev. B* 46 (1992) 6671–6687.
- [42] J.P. Perdew, K. Burke, M. Ernzerhof, Generalized gradient approximation made simple, *Phys. Rev. Lett.* 77 (1996) 3865–3868.
- [43] X.M. Jia, J. Cao, H.L. Lin, M.Y. Zhang, X.M. Guo, S.F. Chen, Transforming type-I to type-II heterostructure photocatalyst via energy band engineering: A case study of I-BiOCl/I-BiOBr, *Appl. Catal. B: Environ.* 204 (2017) 505–514.
- [44] S.Q. Sun, Y.C. Wu, J.F. Zhu, C.J. Lu, Y. Sun, Z. Wang, J. Chen, Stabilizing plasma-induced highly nitrogen-deficient g-C<sub>3</sub>N<sub>4</sub> by heteroatom-refilling for excellent lithium-ion battery anodes, *Chem. Eng. J.* 427 (2022), 131032.
- [45] L.Q. Ye, J.Y. Liu, Z. Jiang, T.Y. Peng, L. Zan, Facets coupling of BiOBr-g-C<sub>3</sub>N<sub>4</sub> composite photocatalyst for enhanced visible-light-driven photocatalytic activity, *Appl. Catal. B: Environ.* 142–143 (2013) 1–7.
- [46] X.N. Hu, Y. Zhang, B.J. Wang, H.J. Li, W.B. Dong, Novel g-C<sub>3</sub>N<sub>4</sub>/BiOCl<sub>1-x</sub>I<sub>x</sub> nanosheets with rich oxygen vacancies for enhanced photocatalytic degradation of organic contaminants under visible and simulated solar light, *Appl. Catal. B: Environ.* 256 (2019), 117789.
- [47] M.M. Zhang, C. Lai, B.S. Li, D.L. Huang, G.M. Zeng, P. Xu, L. Qin, S.Y. Liu, X.G. Liu, H. Yi, M.F. Li, C.C. Chu, Z. Chen, Rational design 2D/2D BiOBr/CDs/g-C<sub>3</sub>N<sub>4</sub> Z-scheme heterojunction photocatalyst with carbon dots as solid-state electron mediators for enhanced visible and NIR photocatalytic activity: Kinetics, intermediates, and mechanism insight, *J. Catal.* 369 (2019) 469–481.
- [48] J. Hu, P. Zhang, W. An, L. Liu, Y. Liang, W. Cui, In-situ Fe-doped g-C<sub>3</sub>N<sub>4</sub> heterogeneous catalyst via photocatalysis-Fenton reaction with enriched photocatalytic performance for removal of complex wastewater, *Appl. Catal. B: Environ.* 245 (2019) 130–142.
- [49] H.W. Huang, Y. He, X.W. Li, M. Li, C. Zeng, F. Dong, X. Du, T.R. Zhang, Y.H. Zhang, Bi<sub>2</sub>O<sub>3</sub>(OH)(NO<sub>3</sub>) as a desirable [Bi<sub>2</sub>O<sub>3</sub>]<sup>2+</sup> layered photocatalyst: Strong intrinsic polarity, rational band structure and {001} active facets co-beneficial for robust photooxidation capability, *J. Mater. Chem. A* 3 (2015) 24547–24556.
- [50] Q. Wang, H. Zhu, B. Li, Synergy of Ti-O-based heterojunction and hierarchical 1D nanobelt/3D microflower heteroarchitectures for enhanced photocatalytic tetracycline degradation and photoelectrochemical water splitting, *Chem. Eng. J.* 378 (2019), 122072.
- [51] X.N. Wang, J.P. Jia, Y.L. Wang, Combination of photocatalysis with hydrodynamic cavitation for degradation of tetracycline, *Chem. Eng. J.* 315 (2017) 274–282.
- [52] Z. Li, X. Wang, N. Xu, Y. Xiao, L. Ma, J. Duan, Cost-effective and visible-light driven melamine-derived sponge for tetracyclines degradation and Salmonella inactivation in water, *Chem. Eng. J.* 394 (2020), 124913.
- [53] Z. Li, C. Guo, J. Lu, Z. Hu, M. Ge, Tetracycline degradation by persulfate activated with magnetic Cu/CuFe<sub>2</sub>O<sub>4</sub> composite: Efficiency, stability, mechanism and degradation pathway, *J. Hazard. Mater.* 373 (2019) 85–96.
- [54] D. Huang, Q. Zhang, C. Zhang, R. Wang, R. Deng, H. Luo, T. Li, J. Li, S. Chen, C. Liu, Mn doped magnetic biochar as persulfate activator for the degradation of tetracycline, *Chem. Eng. J.* 391 (2020), 123532.
- [55] L. Liu, Y. Jiang, H. Zhao, J. Chen, J. Cheng, K. Yang, Y. Li, Engineering coexposed 001 and 101 facets in oxygen-deficient TiO<sub>2</sub> nanocrystals for enhanced CO<sub>2</sub> photoreduction under visible light, *ACS Catal.* 6 (2016) 1097–1108.
- [56] H. Zhao, L. Liu, J.M. Andino, Y. Li, Bicyrystalline TiO<sub>2</sub> with controllable anatase-brookite phase content for enhanced CO<sub>2</sub> photoreduction to fuels, *J. Mater. Chem. A* 1 (2013) 8209–8216.
- [57] S. Cao, Y. Li, B. Zhu, M. Jaroniec, J. Yu, Facet effect of Pd cocatalyst on photocatalytic CO<sub>2</sub> reduction over g-C<sub>3</sub>N<sub>4</sub>, *J. Catal.* 349 (2017) 208–217.
- [58] C. Liu, Z. Han, Y. Feng, H. Dai, Y. Zhao, N. Han, Q. Zhang, Z. Zou, Ultrathin Z-Scheme 2D/2D N-doped HTiNbO<sub>5</sub> nanosheets/g-C<sub>3</sub>N<sub>4</sub> porous composites for efficient photocatalytic degradation and H<sub>2</sub> generation under visible light, *J. Colloid Interface Sci.* 583 (2021) 58–70.